

Comparative analysis of different criteria for the prediction of vortex ring state of floating offshore wind turbines

Dong, Jing; Viré, Axelle

DOI

[10.1016/j.renene.2020.08.027](https://doi.org/10.1016/j.renene.2020.08.027)

Publication date

2021

Document Version

Final published version

Published in

Renewable Energy

Citation (APA)

Dong, J., & Viré, A. (2021). Comparative analysis of different criteria for the prediction of vortex ring state of floating offshore wind turbines. *Renewable Energy*, 163, 882-909.
<https://doi.org/10.1016/j.renene.2020.08.027>

Important note

To cite this publication, please use the final published version (if applicable).
Please check the document version above.

Copyright

Other than for strictly personal use, it is not permitted to download, forward or distribute the text or part of it, without the consent of the author(s) and/or copyright holder(s), unless the work is under an open content license such as Creative Commons.

Takedown policy

Please contact us and provide details if you believe this document breaches copyrights.
We will remove access to the work immediately and investigate your claim.



Comparative analysis of different criteria for the prediction of vortex ring state of floating offshore wind turbines

Jing Dong^{*}, Axelle Viré

Delft University of Technology, Wind Energy Section, Kluyverweg 1, 2629 HS, Delft, the Netherlands



ARTICLE INFO

Article history:

Received 22 April 2020

Received in revised form

17 July 2020

Accepted 8 August 2020

Available online 4 September 2020

Keywords:

Vortex ring state

VRS

Floating offshore wind turbine

FOWT

Unsteady aerodynamics

ABSTRACT

The wind condition around floating offshore wind turbines (FOWTs) can be largely different from that developed around bottom-mounted wind turbines due to the platform motions. The existing literature identifies four working state of FOWTs, one of them being the vortex ring state (VRS) which may occur as the rotor moves in its own wake. It is potentially a problem that influences the aerodynamic performance and lifetime of FOWTs. It is still unclear when, and to what extent, does the VRS happen to floating offshore wind turbines. The aim of this paper is to quantitatively predict the occurrence of VRS during the operation of FOWTs. Three different criteria are used and compared: the axial induction factor, Wolkovitch's criterion and Peters' criterion. The results show that the VRS phenomena may occur for a large range of operating conditions and can be correlated with the minima in the relative wind speed normal to the rotor plane. Also, the probability of occurrence of VRS is smaller for the floating platforms that exhibit the least motions such as the TLP. Finally, Wolkovitch's criterion seems to be the most suitable one for the VRS prediction, while Peters criterion indicates the initial aerodynamic change and is thus suitable for early warning of VRS.

© 2020 The Authors. Published by Elsevier Ltd. This is an open access article under the CC BY license (<http://creativecommons.org/licenses/by/4.0/>).

1. Introduction

In order to significantly increase the share of wind energy produced worldwide, wind energy technology is moving from onshore to offshore and from shallow water to deep water. Floating offshore wind turbines (FOWTs) are expected to be economically better than bottom-mounted turbines when placed in water deeper than 50 m. Despite key initiatives such as the installation of the world's first floating wind farm off the coast of Scotland in 2017, many design challenges need to be solved to make floating offshore wind turbines economically attractive. One of the challenges concerns the complex aerodynamics of FOWTs. Due to the combined effects of wind and waves, FOWTs often experience large amplitude motions. It is shown that a FOWT can be subjected to four working states [1] when the floating platform undergoes pitching motion: windmill state, turbulence state, vortex ring state, and propeller state. The windmill state is the initial operating state, when the turbine extracts energy from the flow field, as shown in the first frame of Fig. 1, where the yellow arrows represent the direction of

the rotor motion. The turbulent state starts when the rotor reaches windward tip and begins to pitch leeward, interacting with its own wake, as shown in the second frame of Fig. 1. The vortex ring state (VRS), or 'settling with power', begins when the relative wind velocity severely drops and a toroidal recirculation flow takes place normal to the rotor disk, as shown in the third frame of Fig. 1. Eventually, the relative wind velocity reverses, and the wind turbine outputs energy in the flow like a propeller, which is the propeller state as shown in the fourth frame of Fig. 1.

For the aero-servo-elastic coupled analysis of bottom-mounted wind turbines or the aero-hydro-servo-elastic coupled analysis of FOWTs, blade element momentum (BEM) [2] and vortex methods [3–5] are preferred over computational fluid dynamics methods for the aerodynamics analysis in order to keep the computational cost relatively low. Despite the shortcomings of BEM, it has low computational cost and can give acceptable accuracy when compared with CFD methods [6,7]. Corrections have been proposed to compensate for the various assumptions of BEM and make it more suitable for some specific real conditions [8].

Generally, when calculating the aerodynamics of onshore wind turbines with BEM theory, only the windmill working state and the turbulent working state (TWS) are considered. This is acceptable because the foundation of bottom-mounted turbines is relatively

^{*} Corresponding author.

E-mail address: j.dong-2@tudelft.nl (J. Dong).

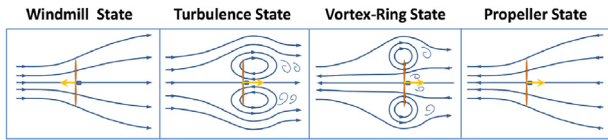


Fig. 1. Four working states of FOWTs (adapted from Sebastian [1]).

stable and the rotor is only subjected to small amplitude vibrations. Thus the VRS and propeller state rarely occur. Glauert’s correction [9] is often used to correct the rotor thrust coefficient when the rotor enters the turbulent state, which can be identified by an induction factor $a > 0.5$. By contrast, the VRS may seriously influence the aerodynamic performance of FOWTs. Leishman [10] reports the effect of the VRS on a helicopter rotor as follows. First, the rotation becomes apparently unsteady and aperiodic. Second, the blades experience successive forward and backward velocities, which can lead to significant blade flapping and a loss of rotor control. Third, the level of thrust fluctuations is high. When the VRS occurs, the momentum theory assumption breaks down and the BEM theory does no longer hold true for the aerodynamic calculation. After Sebastian’s hypothesis [1] that the VRS occurs as a transient phenomenon, several scholars did some research about FOWTs unsteady aerodynamics. Tran [11,12] studied the unsteady aerodynamics of FOWT platform motion using a computational fluid dynamics (CFD) model. Jeon et al. [13] studied the unsteady aerodynamics of FOWTs in platform pitching motion using the vortex lattice method. Kyle [14] researched on the alleviation of the vortex ring state for FOWTs using a modified blade-tip shape based on a CFD method. Additionally, Kyle [15] researched on propeller and vortex ring state of floating offshore wind turbines during surge motion. However, among all the studies about the VRS, two questions have not yet been answered: how often does the VRS happen for FOWTs and to what extent does it occur. The answer to these questions is important to assess if, and how, the VRS should be taken into account in the modeling and design of FOWTs. Moreover, the VRS is a transient phenomenon mainly influenced by the pitch and surge motions of the turbine. Thus the simulation of VRS must be integrated with the simulation of other working states of the wind turbine to assess the aerodynamic response. Traditionally, the unsteady aerodynamic analysis of wind turbines does not distinguish the VRS from the turbulence working state. It does not separately analyze its influence on the rotor either.

So far, there is no special criterion for the prediction of VRS for FOWTs when the rotor interacts with its own wake. However, criteria exist for the prediction of VRS in the context of helicopters during their descent. Basset [16] classified the prediction of the VRS boundaries in three different theories, i.e. zero transport velocity of rotor tip vortices, bifurcation of equilibria, and zero heave damping. Different methods are used to predict the VRS boundaries: Drees [17] identified the VRS as a roughness region based on the ratios between rotorcraft vertical or horizontal velocity and the hover induced velocity. Whashizu [18] experimentally researched on the VRS based on the fluctuation of thrust force. By contrast, Xin and Gao [19] predicted the VRS with model tests taking the torque fluctuation as a reference, while Betzina [20] investigated the VRS with an experimental method taking the decrease of mean thrust as a reference. Wolkovitch [21] and Peters [22] predicted the VRS based on the momentum theory with the assumption that the tip vortices velocity drops to zero. Leishman [23] predicted the VRS based on a free wake vortex method, which shows that the blade-flapping fluctuation can also be a feature of the VRS, besides the thrust and torque fluctuation. In particular, the angle of the blade-flapping fluctuation can be used to predict the VRS onset. Newman

[24] built up a method about the VRS prediction based on the momentum theory, refined using measurement data from Drees [17], and made further reductions based on the nature of the flow in the breakdown regime. Taghizad [25] researched on the VRS with a flight test, during which the VRS boundary was identified with three criteria: first an increase of vibration, followed by a sudden increase in descent rate, and exiting the VRS when the descent rate was stable again. As shown by Basset [16], the different criteria can lead to different VRS boundaries. Generally speaking, the Peters criterion covers relatively larger descent speeds of the rotor than the Wolkovitch criterion.

This paper aims at quantitatively predicting the occurrence of the occurrence of what is commonly referred to as the vortex ring state in the literature on FOWTs supported by different floating foundations. The paper is organized as follows. Section 2 presents the theories used for the prediction of the vortex ring state. Section 3 introduces the simulation tools and the floating offshore wind turbines to be used in the simulation as well as the design load cases. Section 4 presents the VRS prediction results in both regular and irregular wave states. Section 5 summarises the main conclusion and discussion.

2. Theories for the prediction of the vortex ring state

There are numerous prediction methods of the vortex ring state have been developed for the helicopter landing problem. As shown in Fig. 2 [16], nine prediction criteria are listed with uniform pattern coordinates, where the vertical axis represents the non-dimensional relative speed normal to the rotor, the horizontal axis represents the non-dimensional relative speed parallel to the rotor, and the curves forms an envelop of the VRS region in each frame of the diagram. It can be seen that the VRS regions defined by different criteria are significantly different, which is mainly because the aerodynamic phenomenon constantly changes during the development of the VRS and different researchers describe the onset of the VRS differently in their studies. In this paper, we adapt Wolkovitch’s criterion and Peters’ criterion to the study of VRS for FOWTs and compare their performances. These two criteria are chosen as they represent extremes in the prediction of VRS: Wolkovitch predicting the narrowest area and Peters the broadest area of the VRS. The modifications associated with these criteria in the context of wind turbines are presented in this section. Additionally, the VRS prediction based on the axial induction factor a is also first introduced.

2.1. VRS prediction based on the axial induction factor

Fig. 3 shows the rotor states corresponding to the measured thrust coefficient C_T as a function of the axial induction factor a as defined in Eq. (1),

$$V_{rel} = (V_\infty - V_p)(1 - a), \tag{1}$$

where $V_{rel} = V_\infty - V_p + V_i$ is axial relative velocity at the rotor, V_∞ is the free-stream velocity, V_p is the velocity of the platform motion, and V_i is the axial induction at the operating point. From this figure, it can be seen that the vortex ring state is situated between the turbulent wake state and the propeller state, which are separated at $a = 1$. For $a > 1$, Glauert’s empirical relation and the momentum theory are invalid. In the context of wind turbines, the vortices are generated on the blades and shed regularly in the wake, forming vortex rings. The VRS may occur on FOWTs as the rotor can move in its own wake, mainly due to the platform motions such as pitch and surge. At certain times during these motions, the rotor has a downwind speed approximately equal to the traveling speed of the

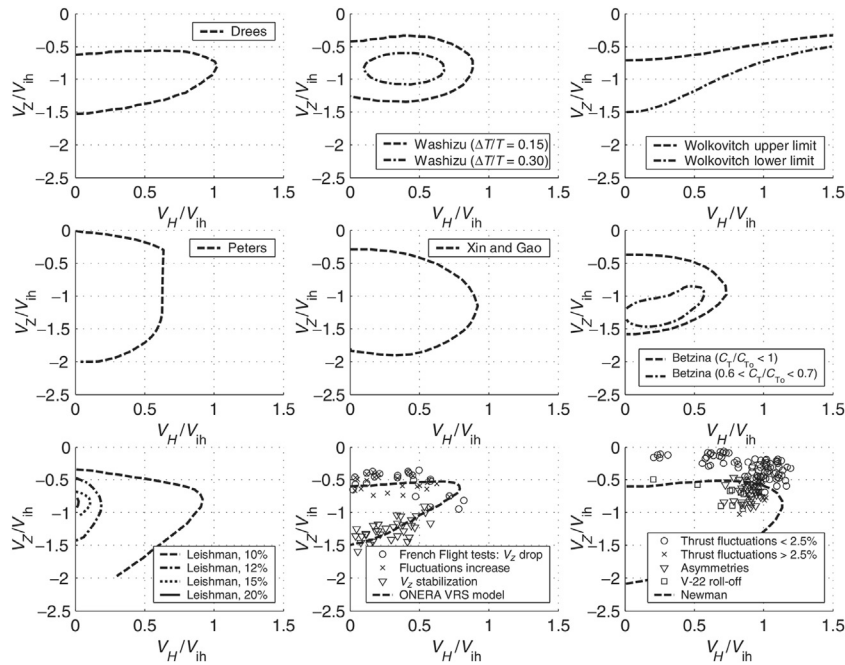


Fig. 2. A summary of VRS boundaries from the literature, where V_Z is the relative speed normal to the rotor, V_H is the relative speed parallel to the rotor, is the rotor-induced velocity at hover [16]. (published with permission).

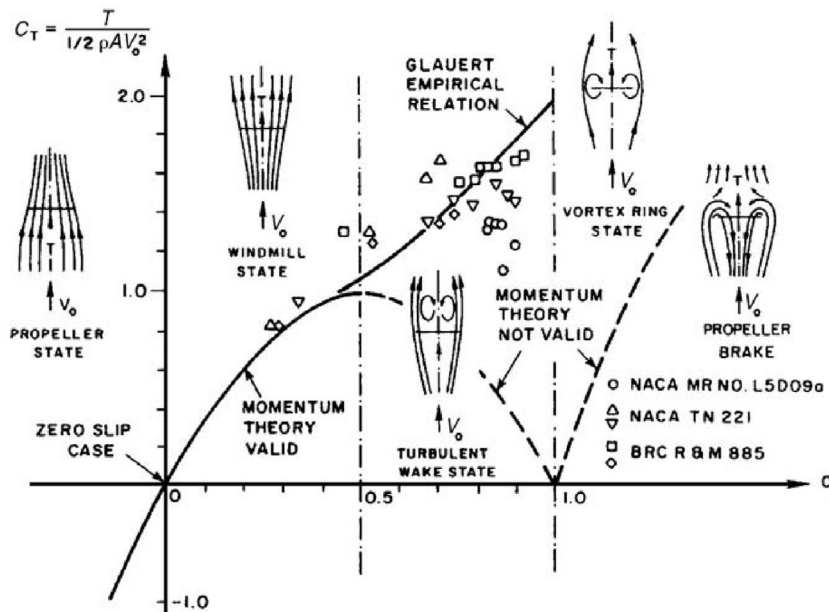


Fig. 3. The rotor states corresponding to the measured thrust coefficient C_T as a function of the axial induction factor a (taken from Ref. [26]).

wake. Following Eq. (1), when $a = 1$, $V_{rel} = 0$. Thus, the value $a = 1$ can be taken as one criterion to predict the VRS.

2.2. VRS prediction based on Wolkovitch criterion

Even if the momentum theory breaks down when the rotor enters the VRS, it can still be used to predict the occurrence of VRS. Wolkovitch [21] developed a method based on the momentum theory and actuator disk concept to predict the vortex ring state during the descent of a powered helicopter. The flow model in this theory can be adapted to wind turbines, as illustrated in Fig. 4, in

which V_R is the wind velocity related to the rotor, V_I is the wake induced velocity at the rotor and α represents the angle between V_R and the rotor disc. The rotor is assumed to be surrounded by a vortex tube. The flow is uniform inside the tube, at any cross section. Outside the tube, the wind speed equals the relative value. This vortex tube is formed of a series of vortex cores. Thus, near the rotor and outside of the tube, the leeward component of the stream velocity is $V_R \sin \alpha$, while inside the tube the windward velocity component is $(V_I - V_R \sin \alpha)$. The velocity of the vortex core center is the average between these velocities, i.e. $(V_I / 2 - V_R \sin \alpha)$, and points in the down-wind direction. The vortex ring state is assumed

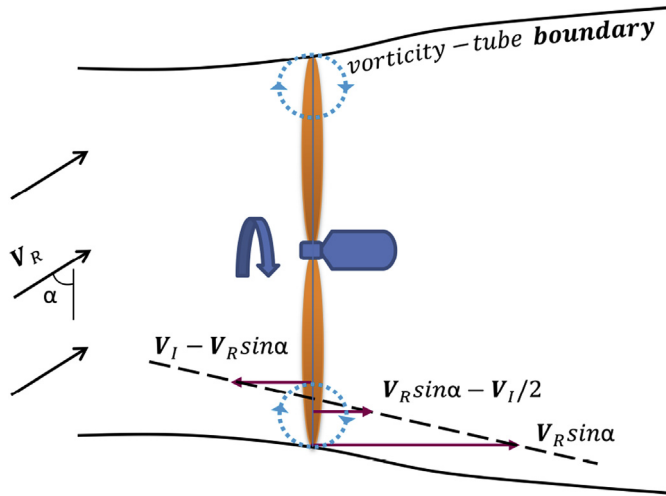


Fig. 4. Illustration of a stream tube and components of the wind speed in the context of the Wolkovitch's model.

to occur when the relative velocity of the vortex cores normal to the rotor disc falls to zero. Thus the critical velocity V_{crit} associated with Wolkovitch's criterion is given by

$$V_{crit} = \frac{V_I}{2 \sin \alpha} \tag{2}$$

When the velocity is smaller than the critical velocity, the rotor is in a vortex ring state. Different criteria predict VRS with different aerodynamic conditions, and Wolkovitch's criterion predicts the VRS onset when the rotor has a speed that can catch up with the core center of the vortex ring.

2.3. VRS prediction based on peters criterion

Peters criterion [22] can be used to predict the VRS of a rotor with both axial and in-plane velocities and was also developed based on the momentum theory. The flow model of this theory adapted to wind turbines is shown in Fig. 5. It can be found that the component of the free stream velocity vector \mathbf{a} in the direction of the wake stream velocity vector \mathbf{b} can be given by

$$\frac{\mathbf{a} \cdot \mathbf{b}}{|\mathbf{b}|} = \frac{\mu^2 + \eta^2 - v\eta}{\sqrt{\mu^2 + (v - \eta)^2}} \tag{3}$$

where η is the non-dimensional axial component of free stream

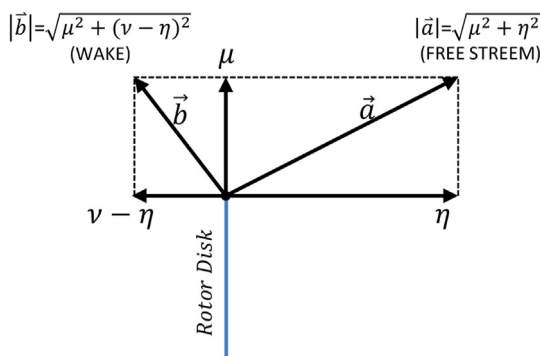


Fig. 5. Illustration of the velocity components in Peters' flow model.

velocity, which is equal to $\mathbf{V}_R \sin \alpha / v_h$, $v_h = \sqrt{C_T} / 2$, C_T is the thrust coefficient; v is the non-dimensional induced velocity, which equals \mathbf{V}_I / v_h , and μ is the non-dimensional inplane component of the free stream velocity.

According to the momentum theory and the flow model, the induce velocity v inside the slipstream can be replaces with κv , where the value κ varies from 1.0 at the rotor disc to 2.0 at infinity [21]. Following the same reasoning as before, i.e. that the averaged velocity inside and outside of the wake should be zero for the VRS to occur, the condition becomes [22].

$$\mu^2 = (\kappa v - \eta) \left(\eta - \frac{\kappa v}{2} \right) = \frac{3}{2} \kappa v \eta - \frac{1}{2} \kappa^2 v^2 - \eta^2, \tag{4}$$

combining with the momentum equation which is given in terms of normalized flow-rates [22].

$$v^2 [\mu^2 + (v - \eta)^2] = 1, \tag{5}$$

the boundary between windmill state and vortex ring state, for the case of $\kappa = 1$, is derived as

$$\mu^2 = \frac{1}{v^2} - \frac{4}{v^6}, \tag{6}$$

$$\eta = v - \frac{2}{v^3}, \tag{7}$$

and the vortex ring boundary from vortex ring state to propeller state, for the case of $\kappa = 2$, is derived as

$$\mu^2 = \frac{1}{v^2} - \frac{1}{v^6}, \tag{8}$$

$$\eta = v + \frac{1}{v^3}. \tag{9}$$

It is worth noting that the two vortex ring boundaries introduced above are opposite to those from the original paper of Peters [22] as the latter deals with helicopters, where the working state of the rotor changes from propeller state to vortex ring state in the near wake and the rotor goes from vortex ring state to windmill state in the far wake. For wind turbines, the near wake and the far wake boundaries are exactly opposite. The influence of wake expansion is always considered in the far wake.

Furthermore, assuming that the vortex ring state occurs when the free stream component along the wake is negative, i.e.

$$\mu^2 + \eta^2 - v\eta < 0, \tag{10}$$

the vortex ring boundary between vortex ring state and

Table 1
Characteristics of the NREL 5 MW reference turbine.

Rating	5 MW
Rotor Orientation, Configuration	Upwind, 3 Blades
Control	Variable Speed, Collective Pitch
Drivetrain	High Speed, Multiple-Stage Gearbox
Rotor, Hub Diameter	126 m, 3 m
Hub Height	90 m
Cut-In, Rated, Cut-Out Wind Speed	3 m/s, 11.4 m/s, 25 m/s
Cut-In, Rated Rotor Speed	6.9 rpm, 12.1 rpm
Rated Tip Speed	80 m/s
Overhang, Shaft Tilt, Precone	5 m, 5°, 2.5°
Rotor Mass	110,000 kg
Nacelle Mass	240,000 kg
Tower Mass	347,460 kg
Coordinate Location of Overall CM	(-0.2 m, 0.0 m, 64.0 m)

Table 2
Characteristics of the three floating platforms.

	MIT/NREL TLP	OC3-Hywind Spar Buoy
Diameter or width * length	18m	6.5–9.4m
Draft	47.89m	120m
Water displacement	12,180 m ³	8029 m ³
Mass, including ballast	8,600,000 kg	7,466,000 kg
CM location below SWL	40.61m	89.92m
Roll inertia about CM	571,600,000 kg·m ²	4,229,000,000 kg·m ²
Pitch inertia about CM	571,600,000 kg·m ²	4,229,000,000 kg·m ²
Yaw inertia about CM	361,400,000 kg·m ²	164,200,000 kg·m ²
Number of mooring lines	8 (4 pairs)	3
Depth to fairleads, anchors	47.89m, 200m	70m, 320m
Radius to fairleads, anchors	27m, 27m	5.2m, 853.9m
Unstretched line length	151.7m	902.2m
Line extensional stiffness	1,500,000,000 N	384,200,000 N
ITI Energy Barge		
Width * length	40m* 40m	
Draft	4m	
Water displacement	6000 m ³	
Mass, including ballast	5,452,000 kg	
CM location below SWL	0.2818m	
Roll inertia about CM	726,900,000 kg·m ²	
Pitch inertia about CM	726,900,000 kg·m ²	
Yaw inertia about CM	1,454,000,000 kg·m ²	
Number of mooring lines	8	
Depth to fairleads, anchors	4m, 150m	
Radius to fairleads, anchors	28.28m, 423.4m	
Unstretched line length	473.3 m	
Line extensional stiffness	589,000,000 N	

windmill state is written as

$$\mu^2 = \frac{1}{\nu^2} - \frac{1}{\nu^6}, \tag{11}$$

$$\eta = \nu - \frac{1}{\nu^3}. \tag{12}$$

Considering that the critical values of μ on the propeller side and on the windmill side should be equal, the final criterion is taken as

$$\mu^2 = \frac{1}{\nu^2} - \frac{1}{\nu^6}, \tag{13}$$

Table 3
Natural frequencies of the three floating platforms [31].

Natural Frequencies of TLP System					
Mode	Frequency[Hz]	Period [s]	Mode	Frequency[Hz]	Period [s]
Surge	0.0165	60.6061	Roll	0.2229	4.4863
Sway	0.0165	60.6061	Pitch	0.2211	4.5228
Heave	0.4375	2.2857	Yaw	0.0972	10.2881
Natural Frequencies of ITI Energy Barge System					
Mode	Frequency[Hz]	Period [s]	Mode	Frequency[Hz]	Period [s]
Surge	0.0076	131.5789	Roll	0.0854	11.7096
Sway	0.0076	131.5789	Pitch	0.0849	11.7786
Heave	0.1283	7.7942	Yaw	0.0198	50.5051
Natural Frequencies of OC3-Hywind System					
Mode	Frequency[Hz]	Period [s]	Mode	Frequency[Hz]	Period [s]
Surge	0.0080	125.0000	Roll	0.0342	29.2398
Sway	0.0080	125.0000	Pitch	0.0343	29.1545
Heave	0.0324	30.8642	Yaw	0.1210	8.2645

$$\eta = \nu \pm \frac{1}{\nu^3}, \tag{14}$$

$$\lambda = \nu - \eta = \mp \frac{1}{\nu^3}. \tag{15}$$

When it is evaluated in the $\mu - \lambda$ plane, the vortex ring state is located inside the envelop of the curve, whilst the upper half represents the boundary with the windmill state and the lower half represents the boundary with the propeller state.

3. Simulation setup and load cases

3.1. Simulation tool

The comprehensive horizontal axis wind turbine simulation code FAST v8 [27] developed by NREL is selected to perform the analysis in this work. This version of FAST drives modules corresponding to different disciplines of the coupled aero-hydro-servo-elastic solution. The aim is to use FAST to output the velocities on the blade sections when the wind turbine is subjected to both wind and waves. These values can be compared to the critical velocities introduced in the previous section, in order to assess whether VRS occurs or not. In this work, the following FAST module are used: AeroDyn v15 to calculate aerodynamic loads based on blade element momentum (BEM) theory and generalized dynamic wake theory [28]; InflowWind for processing wind-inflow including (but not limited to) uniform hub-height wind and full-field (FF) wind generated from TurbSim; HydroDyn to calculate hydrodynamic loads on a structure; MAP++ for mooring loads; ElastoDyn for the structural dynamics; and ServoDyn for control and electrical drive dynamics.

3.2. NREL 5 MW turbine and platforms

The analysis is performed on the NREL offshore 5 MW baseline wind turbine. The basic parameters of the turbine are shown in Table 1, and the reader can refer to the NREL report [29] for more information.

Three types of floaters, namely barge, spar-buoy and TLP, have been modified to support the NREL 5 MW turbine for realistic simulations. The main dimensions and hydrostatic data of these platforms are summarized in Table 2, with the center of mass (CM) defined with respect to the still water level (SWL). The natural

Table 4
Case I: Regular wave + steady wind load cases.

Set A, $\delta = 0.007$						
H (m)	T (s)	Wind Speed (m/s)				
		8	7	6	5	4
10	30.5	LCA-1-1	LCA-2-1	LCA-3-1	LCA-4-1	LCA-5-1
9	28.9	LCA-1-2	LCA-2-2	LCA-3-2	LCA-4-2	LCA-5-2
8	27.2	LCA-1-3	LCA-2-3	LCA-3-3	LCA-4-3	LCA-5-3
7	25.5	LCA-1-4	LCA-2-4	LCA-3-4	LCA-4-4	LCA-5-4
6	23.6	LCA-1-5	LCA-2-5	LCA-3-5	LCA-4-5	LCA-5-5
5	21.5	LCA-1-6	LCA-2-6	LCA-3-6	LCA-4-6	LCA-5-6
4	19.3	LCA-1-7	LCA-2-7	LCA-3-7	LCA-4-7	LCA-5-7
3	16.7	LCA-1-8	LCA-2-8	LCA-3-8	LCA-4-8	LCA-5-8
2	13.6	LCA-1-9	LCA-2-9	LCA-3-9	LCA-4-9	LCA-5-9
1	9.6	LCA-1-10	LCA-2-10	LCA-3-10	LCA-4-10	LCA-5-10
Set B,						
10	25.3	LCB-1-1	LCB-2-1	LCB-3-1	LCB-4-1	LCB-5-1
9	24	LCB-1-2	LCB-2-2	LCB-3-2	LCB-4-2	LCB-5-2
8	22.6	LCB-1-3	LCB-2-3	LCB-3-3	LCB-4-3	LCB-5-3
7	21.1	LCB-1-4	LCB-2-4	LCB-3-4	LCB-4-4	LCB-5-4
6	19.6	LCB-1-5	LCB-2-5	LCB-3-5	LCB-4-5	LCB-5-5
5	17.9	LCB-1-6	LCB-2-6	LCB-3-6	LCB-4-6	LCB-5-6
4	16	LCB-1-7	LCB-2-7	LCB-3-7	LCB-4-7	LCB-5-7
3	13.8	LCB-1-8	LCB-2-8	LCB-3-8	LCB-4-8	LCB-5-8
2	11.3	LCB-1-9	LCB-2-9	LCB-3-9	LCB-4-9	LCB-5-9
1	8	LCB-1-10	LCB-2-10	LCB-3-10	LCB-4-10	LCB-5-10

frequencies of the three floating systems are summarized in Table 3, which were calculated by NREL with an earlier version of FAST [30].

3.3. Design load cases (DLC) and FAST settings

Two types of FAST-simulated DLCs in terms of wind speeds and sea states are listed below. The regular wave load cases aim at assessing the dependence of the VRS with wave and wind parameters. The irregular wave load cases aim at simulating real offshore environmental conditions to see whether the VRS is likely to happen on real wind turbines or not.



Fig. 6. Reference-site location.

3.3.1. Regular wave state

In this group of DLCs, deep-water regular waves [32] are used and zero-degree heading angles are considered for wind, wave and current. The values of the constant wind speed V_∞ and sinusoidal wave with wave height H and wave period T are shown in Table 4. The wind speed range covers the cut-in wind speed and cut-out wind speed of the NREL 5 MW turbine. The wave height range is determined according to the common sea states. The wave period range covers the natural period of the pitch motion of the three floating systems, as shown in Table 3. In order to reduce the set of combined load cases for H , T and V_∞ , the wave steepness δ is considered, i.e.

$$\delta = \frac{H}{cT} = 2\pi \frac{H}{gT^2}, \tag{16}$$

where c is the wave speed and g is the acceleration of gravity taken as 9.8 m/s^2 . Since the FAST hydrodynamic solver HydroDyn assumes linear wave theory [31], the present load cases are limited to $\delta \leq 0.011$ (see Figs. 3 and 4 in ‘DNVGL-RP-C205’ [33]). In Table 4 two sets of load cases are given: in set A, $\delta = 0.007$, the load cases are marked by ‘LCA-m-n’, and in set B, $\delta = 0.01$, the load cases are marked by ‘LCB-m-n’, where ‘m’ and ‘n’ are the serial numbers of the wind speeds and the wave height respectively. The NREL 5 MW turbine supported by a OC3-Hywind spar buoy is selected for the simulation with the regular wave load cases.

3.3.2. Irregular wave state

With irregular waves, we consider the NREL 5 MW turbine supported by three different floaters, namely MIT/NREL TLP, ITI Energy Barge and OC3-Hywind Spar Buoy. The IEC design standard prescribes numerous DLCs. Here, in the power production situation, one set of fatigue-type DLCs (NTM + NSS) and one set of ultimate-type DLCs (NTM + ESS) are considered, where NTM stands for normal turbulence wind model, NSS is the normal sea state wave model and ESS is the extreme sea state wave model [34]. The other DLCs described in the design standards with idling or fault of the turbine are disregarded.

Table 5
Case II: Irregular wave + full field wind load cases.

NTM + NSS															
	LC1	LC2	LC3	LC4	LC5	LC6	LC7	LC8	LC9	LC10	LC11	LC12	LC13	LC14	LC15
V_{∞} (m/s)	4.2	5.6	7.0	8.4	9.8	11.2	12.6	14	15.4	16.8	18.2	19.6	21.0	22.4	23.8
H_s (m)	1.7	1.8	1.9	2.0	2.2	2.4	2.7	3.0	3.4	3.7	4.1	4.5	4.8	5.2	5.5
T_p (s)	12.7	12.7	12.8	14.8	14.1	13.4	12.7	12.1	13.4	13.4	15.5	14.1	13.4	16.2	15.5
NTM + ESS 1-YEAR															
	LC16	LC17	LC18	LC19	LC20	LC21	LC22	LC23	LC24	LC25	LC26	LC27	LC28	LC29	LC30
V_{∞} (m/s)	4.2	5.6	7.0	8.4	9.8	11.2	12.6	14.0	15.4	16.8	18.2	19.6	21.0	22.4	23.8
H_{s1} (m)	10.8	10.8	10.8	10.8	10.8	10.8	10.8	10.8	10.8	10.8	10.8	10.8	10.8	10.8	10.8
T_{p1} (s)	17.6	17.6	17.6	17.6	17.6	17.6	17.6	17.6	17.6	17.6	17.6	17.6	17.6	17.6	17.6
NTM + ESS 50-YEAR															
	LC31	LC32	LC33	LC34	LC35	LC36	LC37	LC38	LC39	LC40	LC41	LC42	LC43	LC44	LC45
(m/s)	4.2	5.6	7.0	8.4	9.8	11.2	12.6	14.0	15.4	16.8	18.2	19.6	21.0	22.4	23.8
H_{s50} (m)	13.8	13.8	13.8	13.8	13.8	13.8	13.8	13.8	13.8	13.8	13.8	13.8	13.8	13.8	13.8
T_{p50} (s)	19.2	19.2	19.2	19.2	19.2	19.2	19.2	19.2	19.2	19.2	19.2	19.2	19.2	19.2	19.2

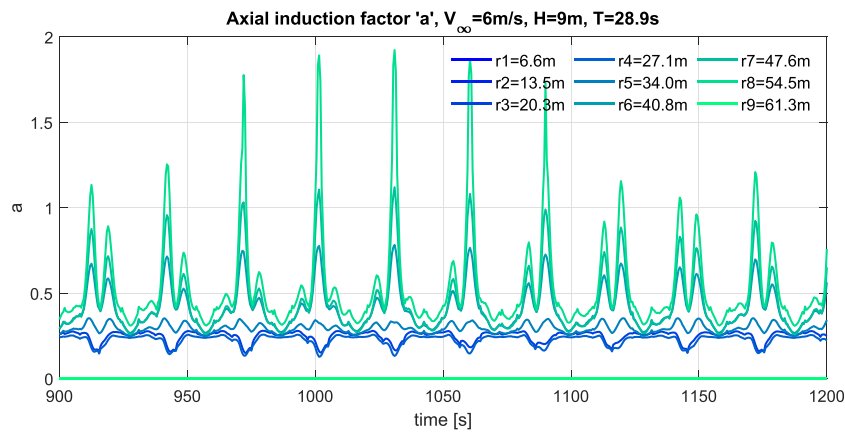


Fig. 7. Values of the axial induction factor a on the different blade nodes (LCA–3–2), (r_{1-9} indicates the location on the blade starting from the root).

According to the requirement of the IEC 61400-3 design standard, the loads analysis shall be based on site-specific external conditions. The test site is located at $61^{\circ} 20' N$ latitude, $0^{\circ} 0' E$ longitude on the prime meridian northeast of the Shetland Islands,

the northeast of Scotland, as illustrated in Fig. 6. The environment data as shown in Table 5 was extracted from the NREL technical report [35] at the same location. The NTM + NSS data set is the long-term joint-probability distribution of wind speed V_{∞} ,

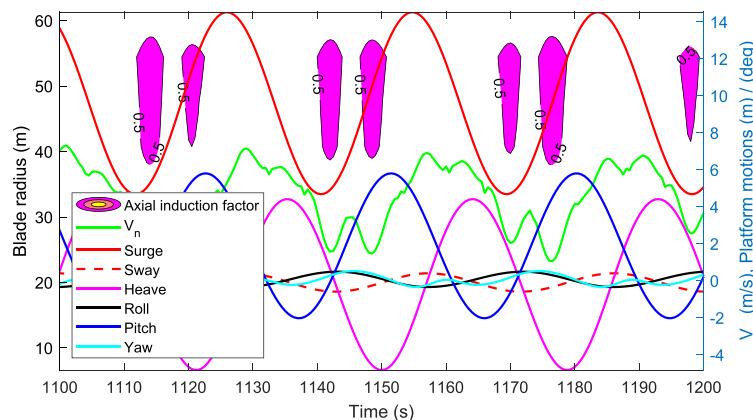


Fig. 8. Regions of VRS predicted with 'a' (in yellow) together with V_n and platform motions (LCA–2–2). (For interpretation of the references to color in this figure legend, the reader is referred to the Web version of this article.)

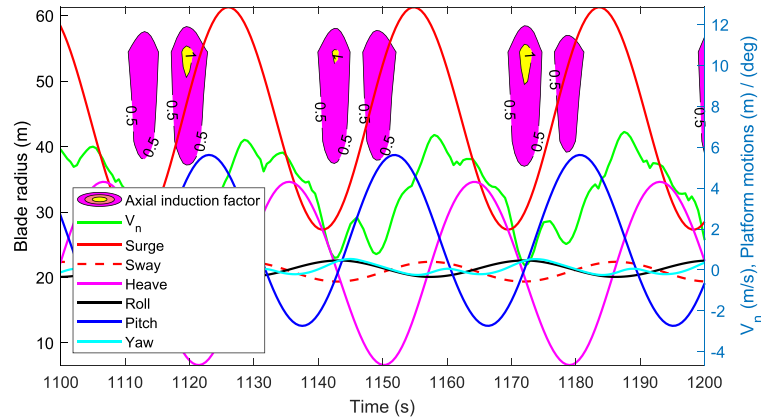


Fig. 9. Regions of VRS predicted with 'a' (in yellow) together with V_n and platform motions (LCA–3–2). (For interpretation of the references to color in this figure legend, the reader is referred to the Web version of this article.)

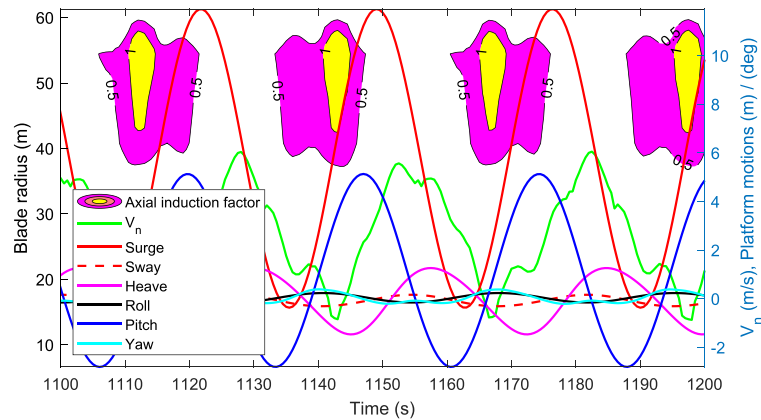


Fig. 10. Regions of VRS predicted with 'a' (in yellow) together with V_n , platform motions (LCA–4–3). (For interpretation of the references to color in this figure legend, the reader is referred to the Web version of this article.)

significant wave height H_s , and peak-spectral period of incident waves T_p . The NTM + ESS data set is the extreme waves with a 1-year return period (H_{s1}, T_{p1}) and a 50-year return period (H_{s50}, T_{p50}), respectively. The fifteen wind speeds of the NTM + NSS data

set are also used for the calculations with the extreme wave data (NTM + ESS set).

The default settings in FAST for these simulations are the following. The 6-DOFs platform motions are switched on. The

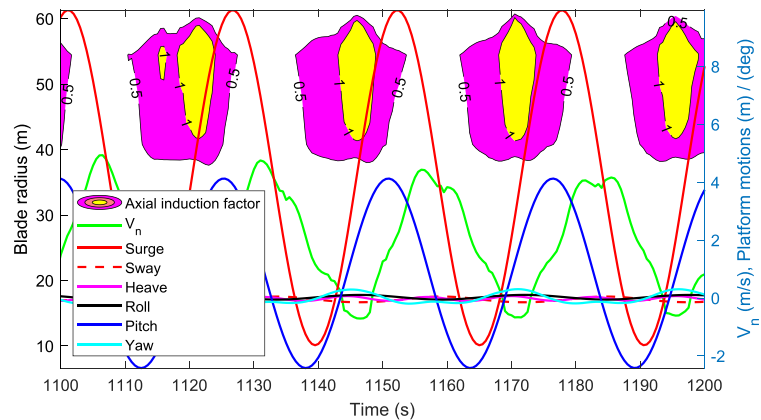


Fig. 11. Regions of VRS predicted with 'a' (in yellow) together with V_n and platform motions (LCA–5–4). (For interpretation of the references to color in this figure legend, the reader is referred to the Web version of this article.)

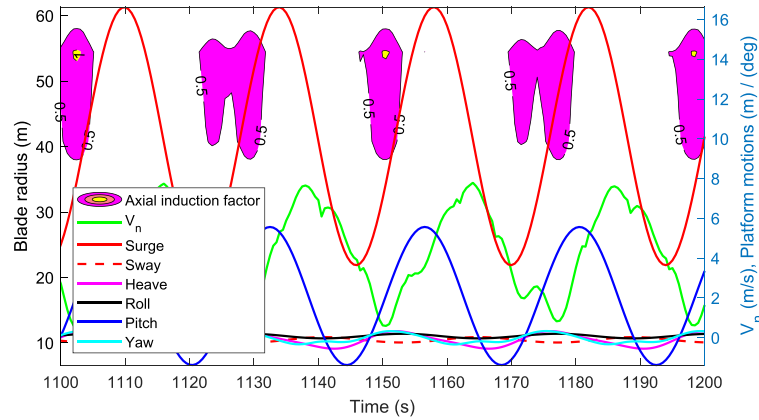


Fig. 12. Regions of VRS predicted with 'a' (in yellow) together with V_n and platform motions (LCB–2–2). (For interpretation of the references to color in this figure legend, the reader is referred to the Web version of this article.)

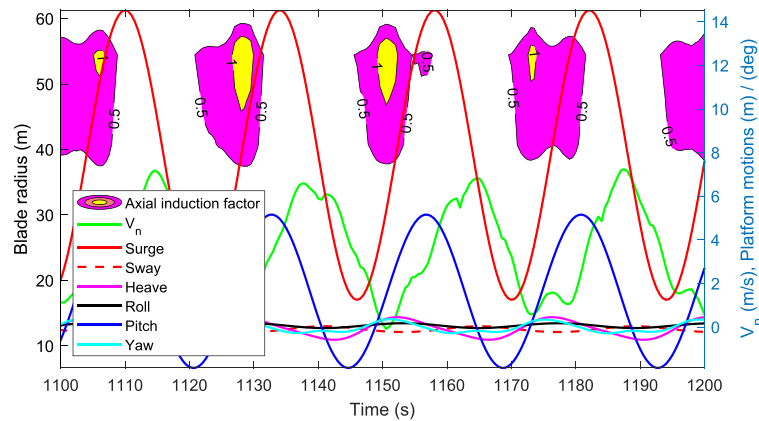


Fig. 13. Regions of VRS predicted with 'a' (in yellow) together with V_n and platform motions (LCB–3–2). (For interpretation of the references to color in this figure legend, the reader is referred to the Web version of this article.)

tower and blades are considered as rigid. For Case I, the free stream wind is defined as constant, unidirectional and without shear, while for Case II, the free stream wind is defined as a full-field 3-component stochastic wind. The blade airfoil aerodynamics model is Beddoes-Leishman (B-L) model and the

unsteady airfoil aerodynamic (UA) model is the B-L model developed by Minnema/Pierce. The blade pitch and electrical-drive dynamics control are switched on. The total simulation time is set to 1200s. The initial 300s of each simulation are omitted in the analysis.

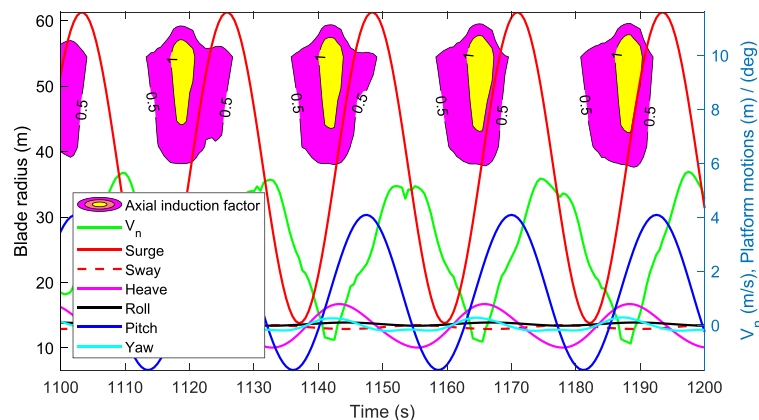


Fig. 14. Regions of VRS predicted with 'a' (in yellow) together with V_n and platform motions (LCB–4–3). (For interpretation of the references to color in this figure legend, the reader is referred to the Web version of this article.)

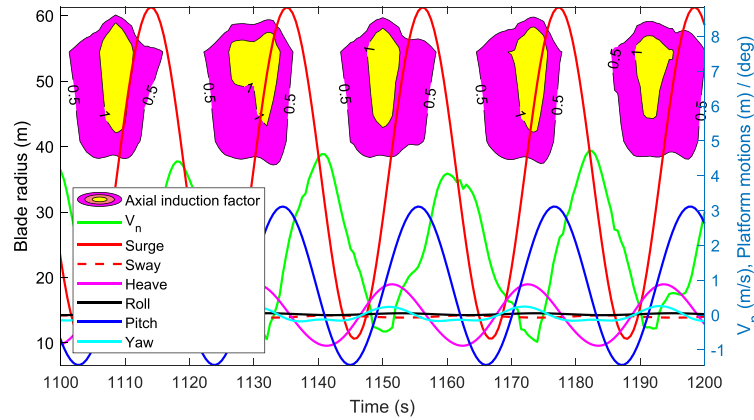


Fig. 15. Regions of VRS predicted with 'a' (in yellow) together with V_n and platform motions (LCB–5–4). (For interpretation of the references to color in this figure legend, the reader is referred to the Web version of this article.)

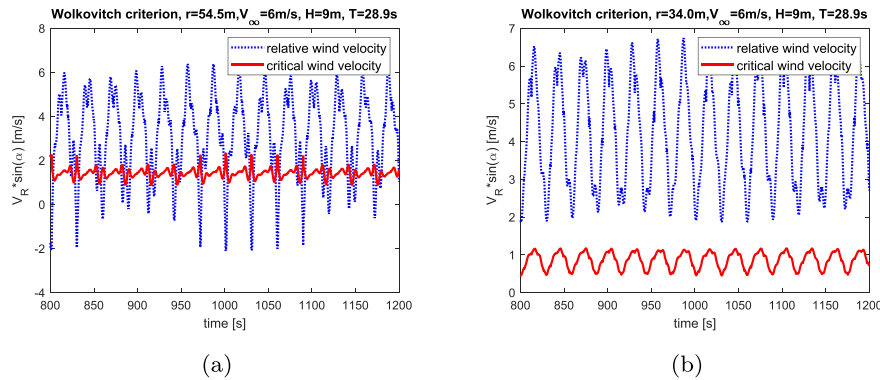


Fig. 16. VRS predicted with 'w' on two different blade nodes of the OC3 wind turbine: (a) node $r = 54.5m$, (b) $r = 34m$.

4. Results and discussion

4.1. Regular wave load cases

4.1.1. Results using the axial induction factor criterion

In this section, the criterion based on the axial induction factor a , abbreviated as 'a', as introduced in section 2.1, is used for the

prediction of the VRS. An example of the time history curves of a from FAST v8 for 9 nodes spread equally along the blade of the OC3 Spar wind turbine is shown in Fig. 7. Due to tip loss and hub loss settings in FAST, the blade nodes r1, r2 on the root and r9 on the tip only have zero values of a . At the other blade nodes, a is positive and increases towards the blade tip. Fig. 7 shows that, for the load case $V_\infty = 6m/s$, $H = 9m$, $T = 28.9s$, the blade nodes $r7 = 47.6m$

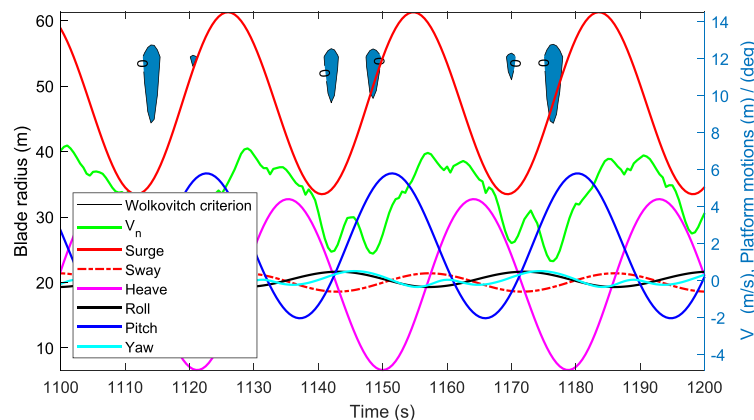


Fig. 17. Regions of VRS according to 'w' (in blue) together with V_n and platform motions (LCA–2–2). (For interpretation of the references to color in this figure legend, the reader is referred to the Web version of this article.)

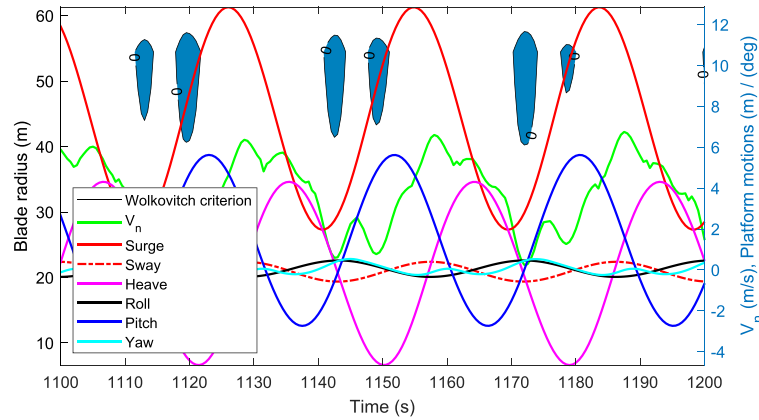


Fig. 18. Regions of VRS according to 'w' (in blue) together with V_n and platform motions (LCA–3–2). (For interpretation of the references to color in this figure legend, the reader is referred to the Web version of this article.)

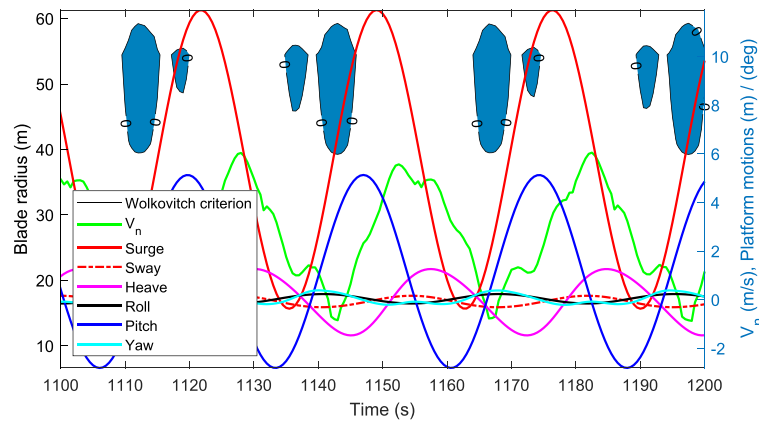


Fig. 19. Regions of VRS according to 'w' (in blue) together with V_n and platform motions (LCA–4–3). (For interpretation of the references to color in this figure legend, the reader is referred to the Web version of this article.)

and $r8 = 54.5\text{m}$ exhibit $a > 1$ at certain times, which is considered to be in the VRS, while the blade nodes $r6 = 40.8\text{m}$, $r7 = 47.6\text{m}$ and $r8 = 54.5\text{m}$ have $0.5 < a < 1$, which is in turbulent state.

Due to a sheer volume of results, only a small fraction is presented here. Eight samples of the VRS prediction results are shown from Fig. 8 to Fig. 15. All the figures are obtained with the same value of wind speeds and wave heights but differ in wave steepness. For the first four figures, $\delta = 0.007$ whilst for the next four figures, $\delta = 0.01$. The area colored in red represent $0.5 < a < 1$ and the area colored in yellow color represent $a \geq 1$, corresponding to the occurrence of VRS. The relative wind speed normal to the rotor plane V_n and the 6-degree of freedom platform motions are plotted as reference, with the values shown on the right-hand-side vertical axis. The V_n curve represented by the green line directly determines the VRS prediction result which is a combined effect of the 6-Dof platform motions. The surge and pitch motions of the platform which are represented by the red line and the blue line, respectively, dominate the rotor motion along the wind direction. From the figures, it can be found that the VRS ($a \geq 1$) areas are surrounded by the TWS ($a \geq 0.5$) areas, with the TWS area being larger than the VRS area in both blade radial span and time span. The VRS only shows on the outboard part of the blade, except at the tip due to the tip-loss correction of the BEM theory. From Figs. 8–11, it can be seen that the VRS area becomes larger when the wind speed

decreases. Furthermore, for identical values of wind speed and wave height, the VRS areas are wider for larger values of the wave steepness. Also, the VRS occurs periodically when V_n is negative. In some cases, such as in Figs. 8 and 9, there are two centers of the VRS in one period, and V_n is negative in two regions correspondingly (see Fig. 12) (see Fig. 13) (see Fig. 14) (see Fig. 10).

4.1.2. Results using Wolkovitch's criterion

Wolkovitch's criterion, abbreviated as 'w', as introduced in

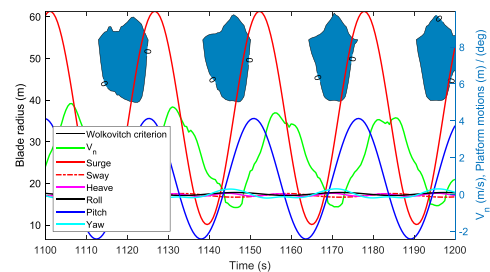


Fig. 20. Regions of VRS according to 'w' (in blue) together with V_n and platform motions (LCA–5–4). (For interpretation of the references to color in this figure legend, the reader is referred to the Web version of this article.)

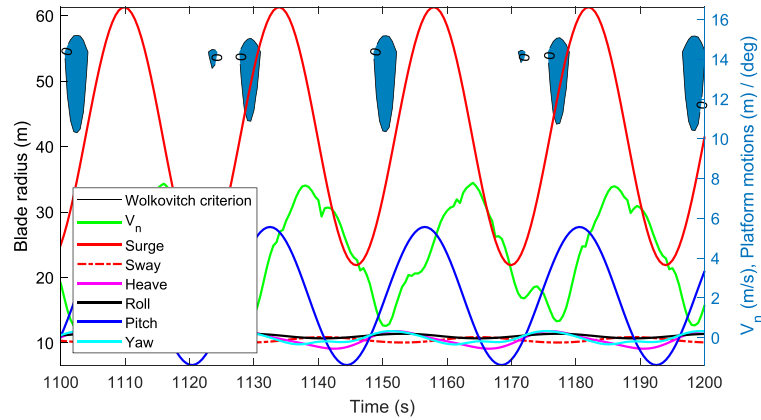


Fig. 21. Regions of VRS according to 'w' (in blue) together with V_n and platform motions (LCB–2–2). (For interpretation of the references to color in this figure legend, the reader is referred to the Web version of this article.)

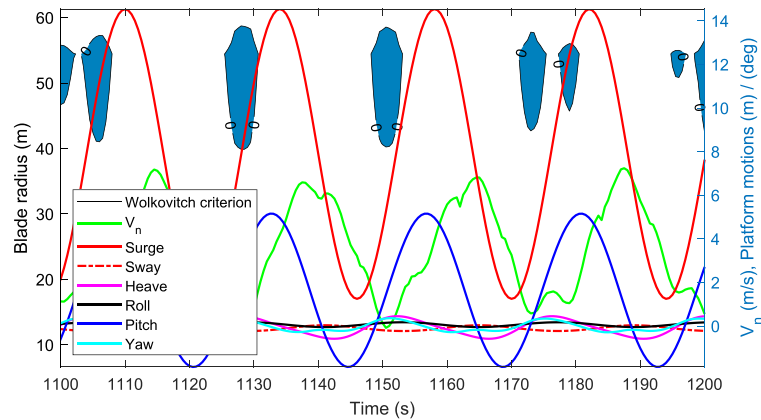


Fig. 22. Regions of VRS according to 'w' (in blue) together with V_n and platform motions (LCB–3–2). (For interpretation of the references to color in this figure legend, the reader is referred to the Web version of this article.)

section 2.2, uses an axial velocity parameter to predict the VRS. The examples of the VRS prediction results according to this criterion on single nodes of a rotor blade are shown in Fig. 16, in which (a) represents a typical case with VRS occurrence and (b) represents a

typical case that the VRS does not occur. The blue dotted lines represent the relative velocities on the blade normal to the rotor disc and the red lines represent the critical velocities calculated based on Wolkovitch's criterion. Thus, when the blue dotted line is

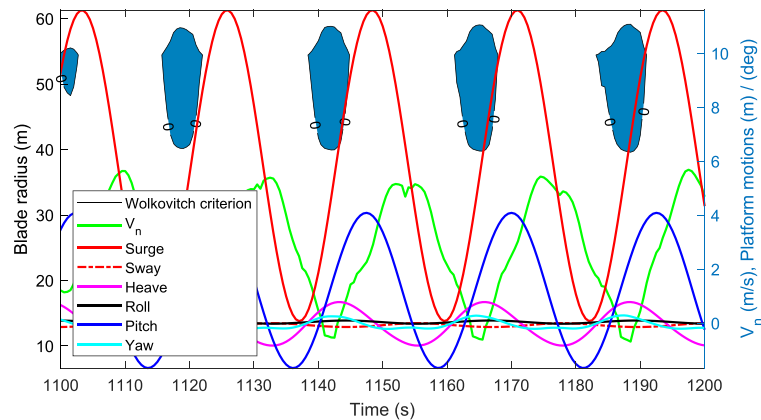


Fig. 23. Regions of VRS according to 'w' (in blue) together with V_n and platform motions (LCB–4–3). (For interpretation of the references to color in this figure legend, the reader is referred to the Web version of this article.)

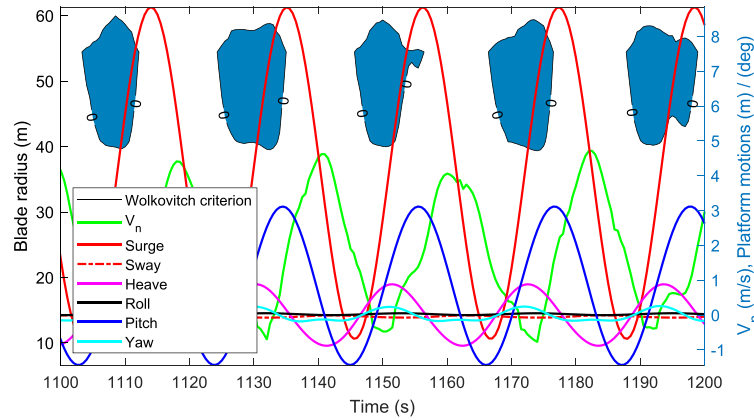


Fig. 24. Regions of VRS according to ‘w’ (in blue) together with V_n and platform motions (LCB–5–4). (For interpretation of the references to color in this figure legend, the reader is referred to the Web version of this article.)

below the red line at a given time, the blade node enters the vortex ring state. It can be seen from Fig. 16a that, at the blade node $r = 54.5\text{m}$, the VRS often occurs when the relative velocities drop

rapidly. Fig. 16b shows that the change in relative velocities is similar than in Fig. 16a. However, the VRS never occurs at that blade node because the amplitude of the critical velocity is smaller than

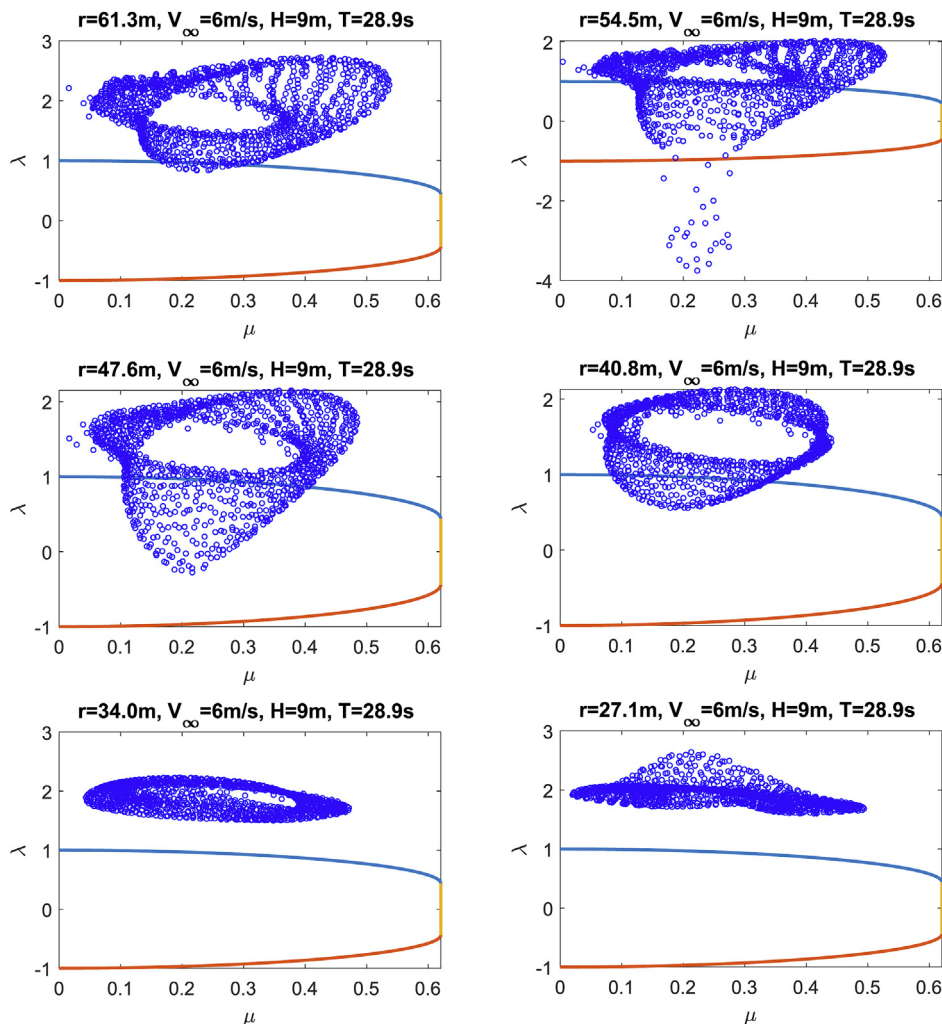


Fig. 25. VRS predicted with ‘p’ criterion on blade nodes of OC3 wind turbine (The blue curve is the VRS boundary to the windmill state, the orange curve is the VRS boundary to propeller state, the yellow line corresponding to $\mu = 0.62$). (For interpretation of the references to color in this figure legend, the reader is referred to the Web version of this article.)

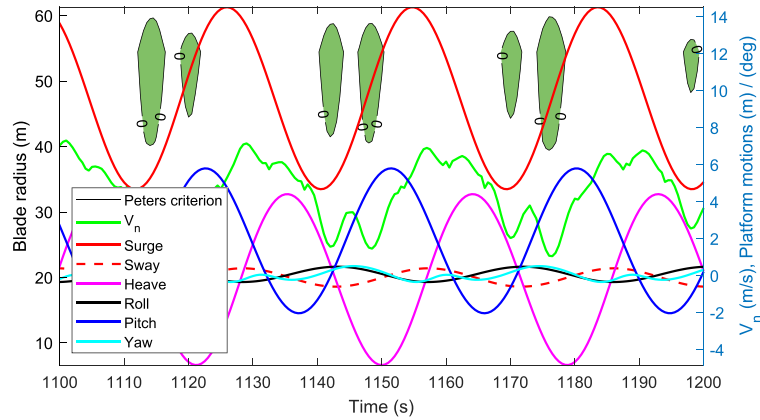


Fig. 26. Regions of VRS according to 'p' (in green) together with V_n and platform motions (LCA–2–2). (For interpretation of the references to color in this figure legend, the reader is referred to the Web version of this article.)

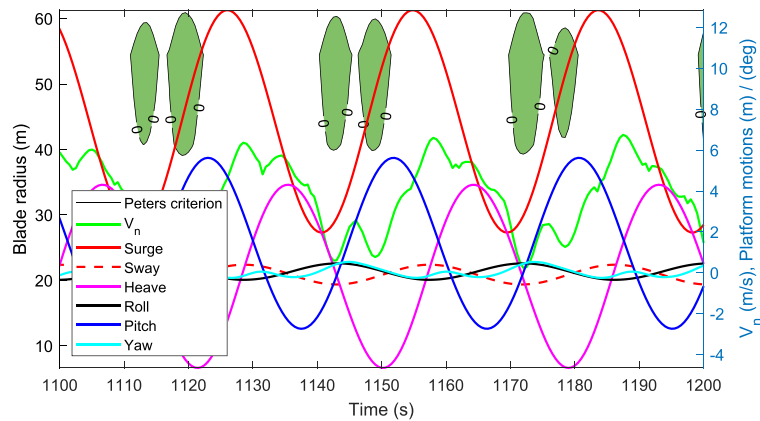


Fig. 27. Regions of VRS according to 'p' (in green) together with V_n and platform motions (LCA–3–2). (For interpretation of the references to color in this figure legend, the reader is referred to the Web version of this article.)

in Fig. 16a, whilst the magnitude of the relative velocity is larger.

Eight samples of the VRS prediction results according to Wolkovitch's criterion along the blade in time domain are shown from Fig. 17–22, with the same load cases as the figures in Section 4.1.1.

The shaded blue area represent the regions of occurrence of VRS according to Wolkovitch's criterion. The relative wind speed normal to the rotor plan V_n and the 6-degree of freedom platform motions are plotted for reference, with their values shown on the

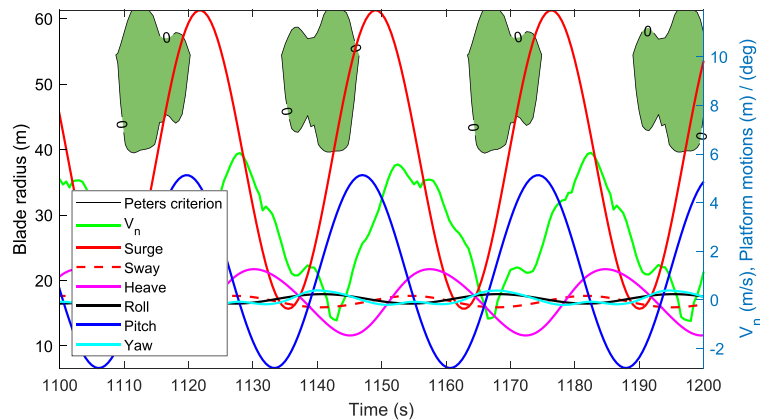


Fig. 28. Regions of VRS according to 'p' (in green) together with V_n and platform motions (LCA–4–3). (For interpretation of the references to color in this figure legend, the reader is referred to the Web version of this article.)

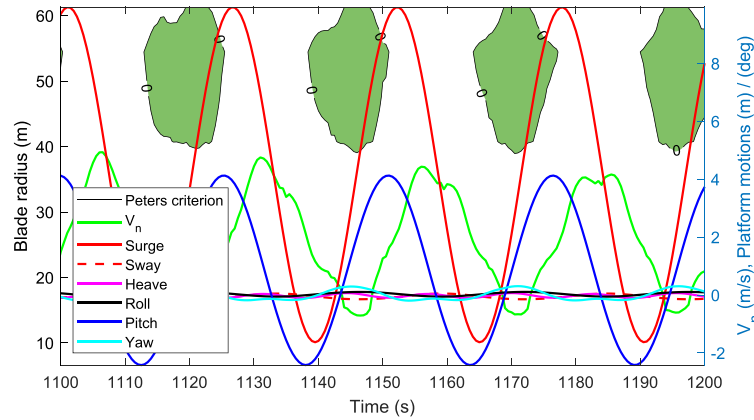


Fig. 29. Regions of VRS according to 'p' (in green) together with V_n and platform motions (LCA–5–4). (For interpretation of the references to color in this figure legend, the reader is referred to the Web version of this article.)

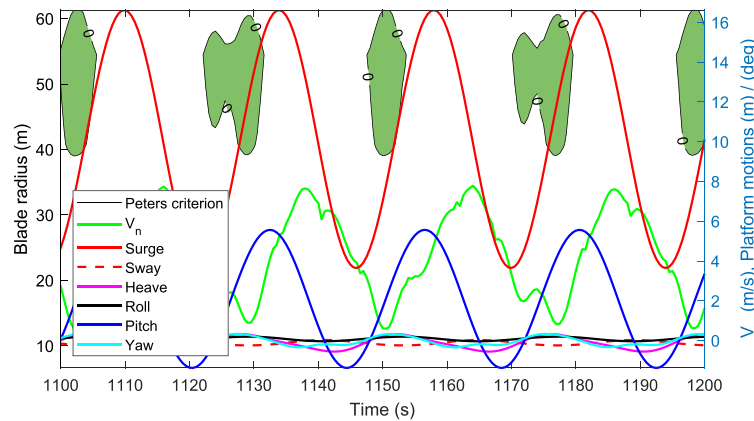


Fig. 30. Regions of VRS according to 'p' (in green) together with V_n and platform motions (LCB–2–2). (For interpretation of the references to color in this figure legend, the reader is referred to the Web version of this article.)

vertical axis on the right-hand-side. Although the exact regions of VRS differ from those obtained with the criterion based on the induction factor, similar observations can be made. In particular, the VRS area increase when the wind speed decreases and widen as δ increases. Also, the VRS occurs periodically when V_n reaches its minimum values. In some cases, such as Figs. 17, Figs. 18 and 19, the VRS occurs twice within a short period of time, which is because V_n has two valley points due to the phase differences of the surge and pitch motions of the platform. By contrast, Fig. 20 shows one large area of occurrence of VRS per period of the platform motion, mainly because the surge and pitch motions have relatively small phase differences in this load case. It can also be found that the VRS area predicted with 'w' totally covers the area of $a \geq 0$ in Section 4.1.1 (see Fig. 23) (see Fig. 24).

4.1.3. Results using Peters' criterion

Peters' criterion, abbreviated as 'p', as introduced in Section 2.3, uses one axial velocity parameter and one inplane velocity parameter to predict the VRS. Examples of the VRS prediction results according to 'p' on single nodes of a rotor blade are shown in Fig. 25. The blue points in each subfigure represent a set of non-dimensional coordinates of (μ, λ) on a particular blade node, in a certain period of time, and the solid curves represent the critical velocities given by 'p'. When a blue point is located inside the

region enclosed by the curves $\lambda = \pm \frac{1}{\mu^3}$ ($0 \leq \mu \leq 0.62$) in the plane, the blade node is considered to be in the vortex ring state. Fig. 25 shows that the VRS does not occur on the two blade nodes located at $r = 27.1\text{m}$ and $r = 34.0\text{m}$, as all the blue points fall outside of the region of interest. For the two blade nodes located at $r = 40.8\text{m}$ and $r = 47.6\text{m}$, the sets of (μ, λ) go across the upper branch of λ critical values and fall into the VRS region. The blade node $r = 47.6\text{m}$ has some negative values of λ , whilst the blade node

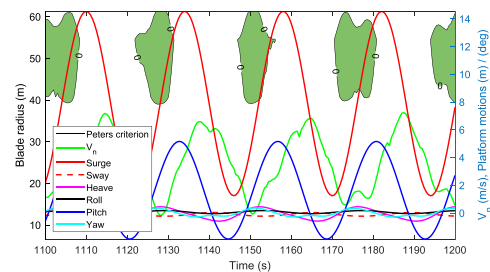


Fig. 31. Regions of VRS according to 'p' (in green) together with V_n and platform motions (LCB–3–2). (For interpretation of the references to color in this figure legend, the reader is referred to the Web version of this article.)

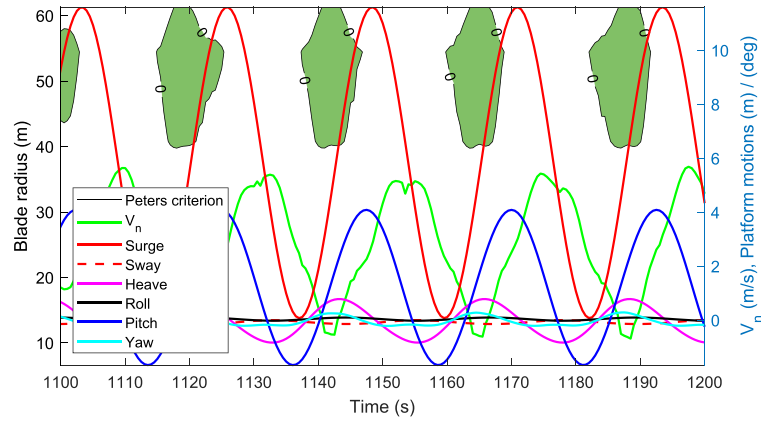


Fig. 32. Regions of VRS according to 'p' (in green) together with V_n and platform motions (LCB–4–3). (For interpretation of the references to color in this figure legend, the reader is referred to the Web version of this article.)

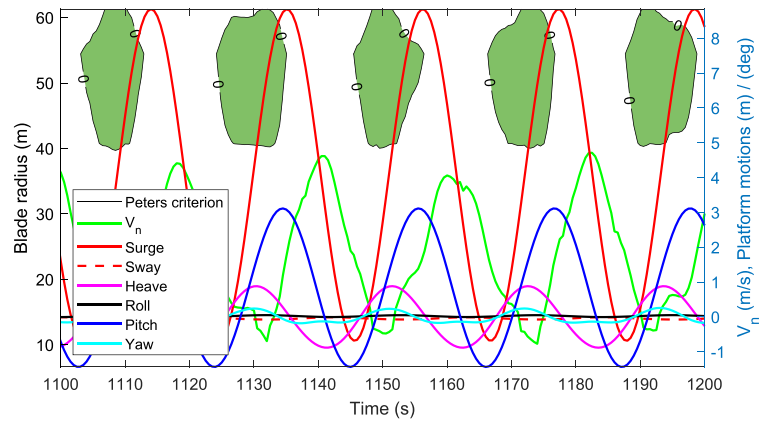


Fig. 33. Regions of VRS according to 'p' (in green) together with V_n and platform motions (LCB–5–4). (For interpretation of the references to color in this figure legend, the reader is referred to the Web version of this article.)

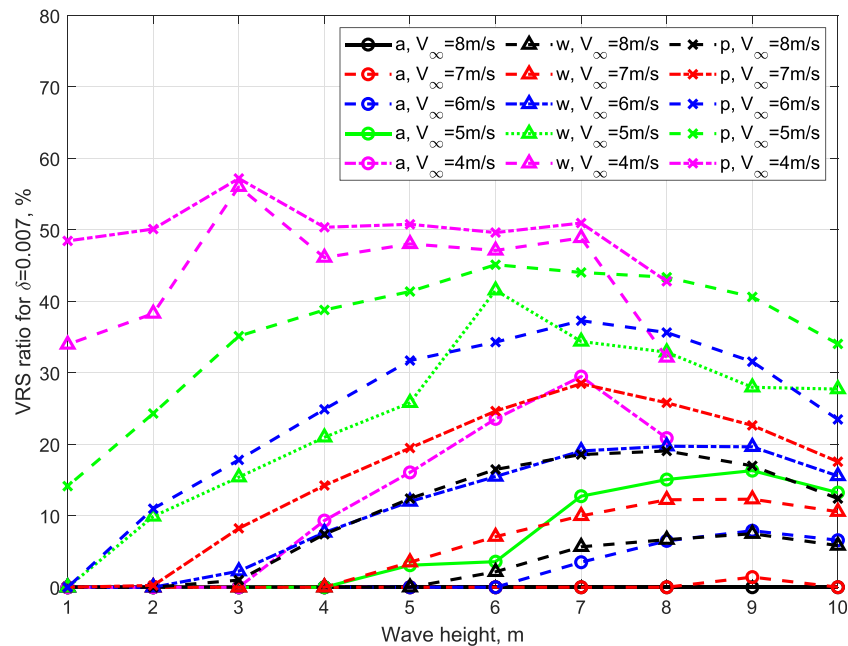


Fig. 34. Percentages of occurrence of the VRS for a time interval of 1200s and a wave steepness $\delta = 0.007$.

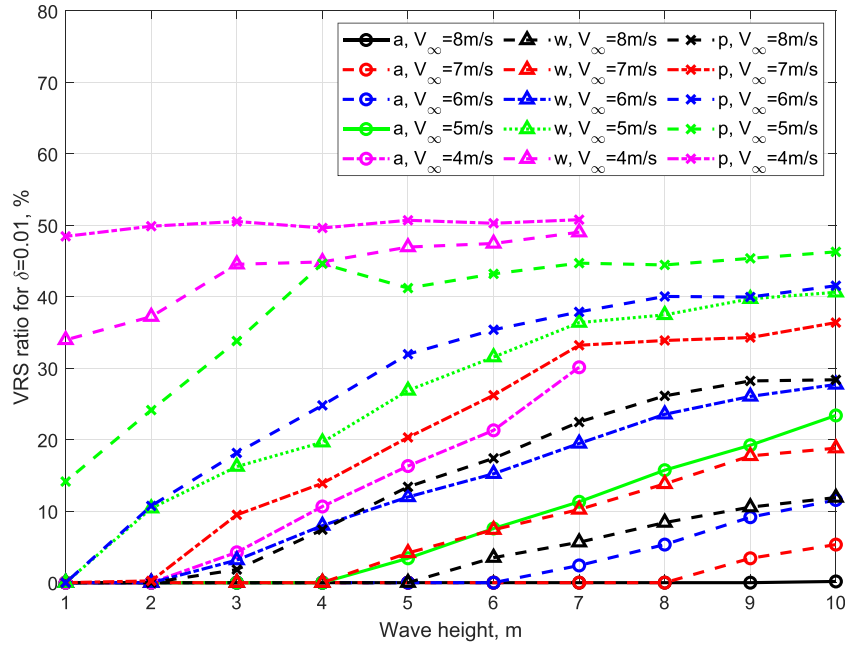


Fig. 35. Percentages of occurrence of the VRS for a time interval of 1200s and a wave steepness $\delta = 0.01$.

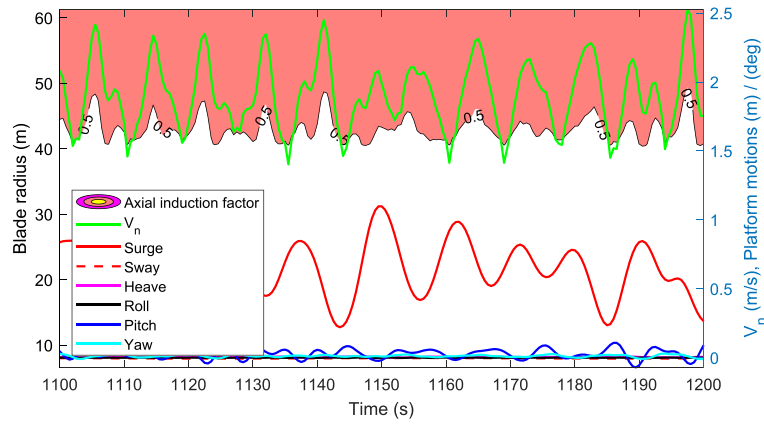


Fig. 36. TLP with irregular waves (LC1): VRS predicted with 'a'.

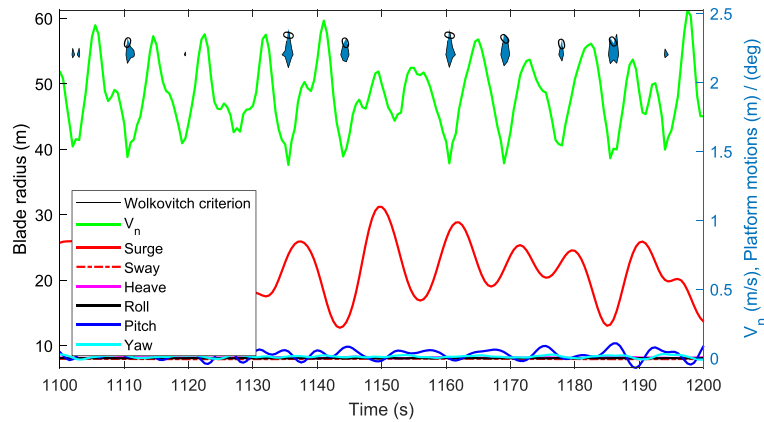


Fig. 37. TLP with irregular waves (LC1): VRS predicted with 'w'.

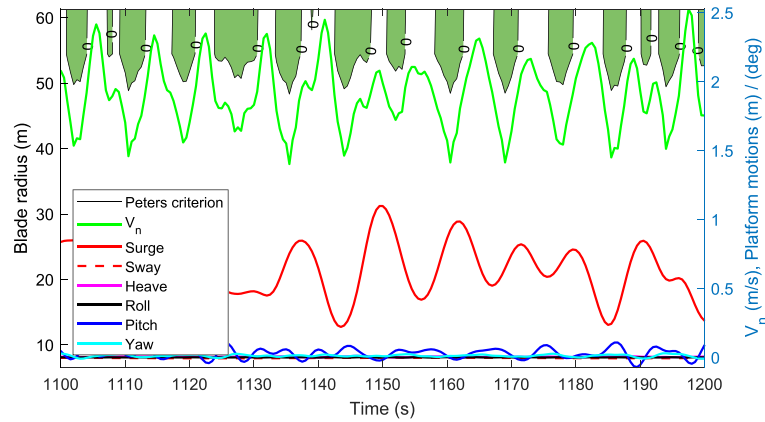


Fig. 38. TLP with irregular waves (LC1): VRS predicted with 'p'.

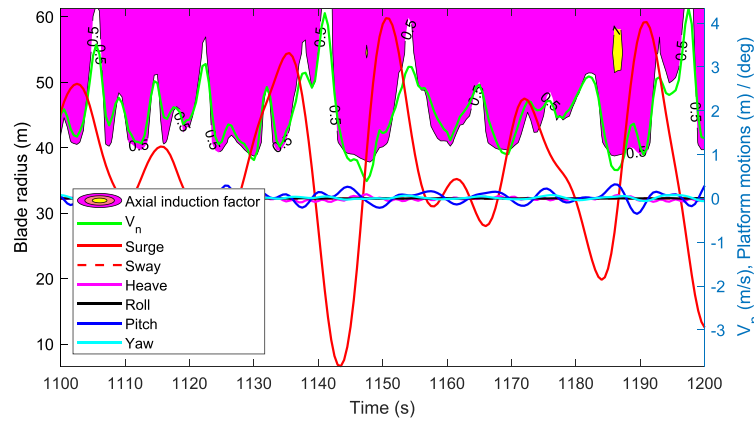


Fig. 39. TLP with irregular waves (LC16): VRS predicted with 'a'.

$r = 40.8\text{m}$ has only positive values of λ . Moreover, the VRS is wider at $r = 47.6\text{m}$ than at $r = 40.8\text{m}$, which is mainly because the pitch motion of the platform can occasionally cause larger leeward velocities on the outboard part of the blade while the rotor rotates. The blade node located at $r = 54.5\text{m}$ is the only one that has a set of (μ, λ) that goes across both the upper branch and the lower branch

of the critical values of λ . It also has the largest proportion of VRS among all the six blade nodes. The blade node located at $r = 61.3\text{m}$ also has a set of (μ, λ) that goes across the upper branch of the critical values. However, it exhibits a smaller proportion of VRS due to the tip loss corrections effect. Among all the six blade nodes, $\mu \leq 0.6$ which is relatively small because only zero degree heading

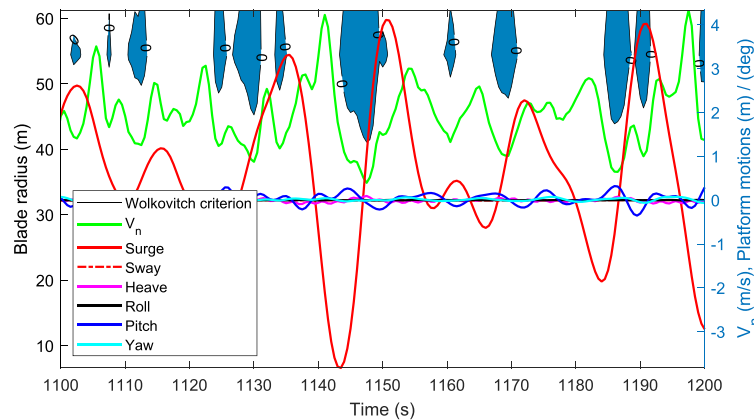


Fig. 40. TLP with irregular waves (LC16): VRS predicted with 'w'.

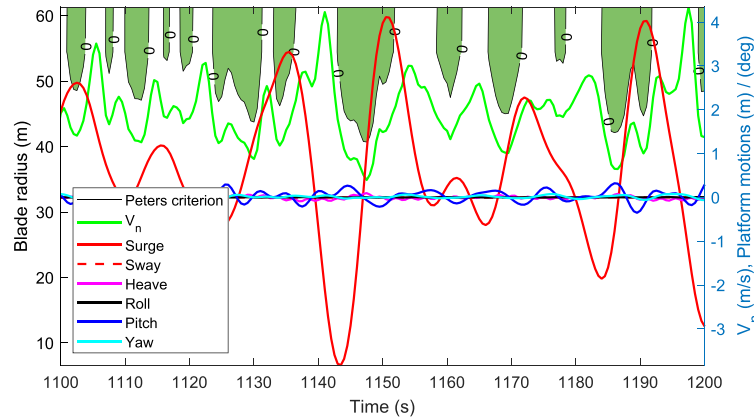


Fig. 41. TLP with irregular waves (LC16): VRS predicted with 'p'.

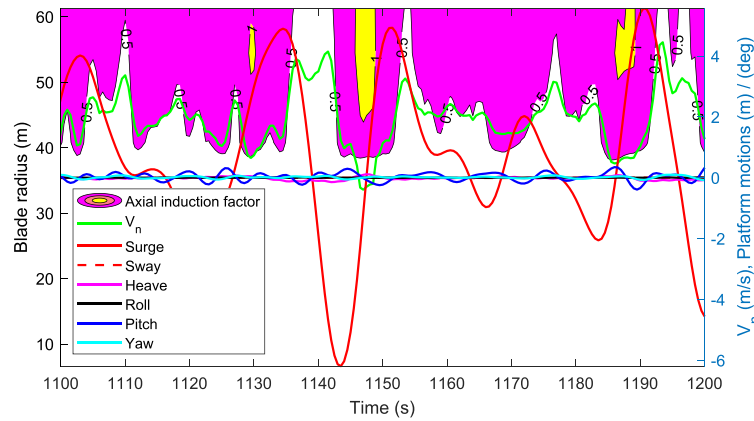


Fig. 42. TLP with irregular waves (LC31): VRS predicted with 'a'.

angles for wind, wave and current are considered in the design load case.

Eight samples of the VRS predicted with 'p' along the blade in time domain are shown from Fig. 26 to Fig. 33, with the same load cases as in the two previous sections. The green shaded area represent the region of occurrence of the VRS as predicted by 'p'.

The relative wind speed normal to the rotor plan V_n and the 6-degree of freedom platform motions are plotted as reference, with their values shown on the vertical axis on the right-hand-side. The figures show that the VRS only occurs are the outboard part of the blade and the VRS regions narrow down near the blade tip. The VRS occurs when the FOWT has leeward platform motions, which

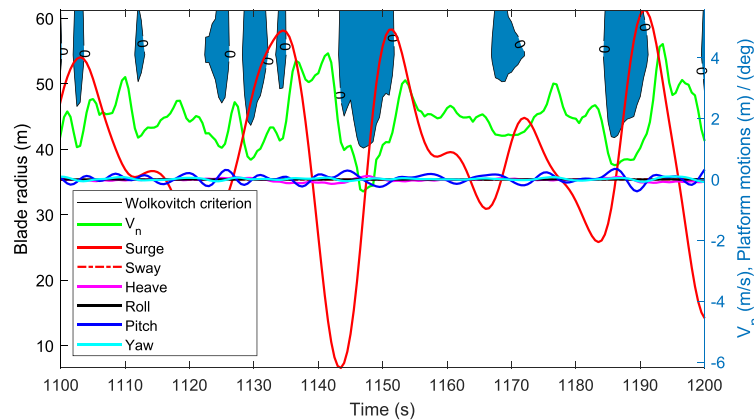


Fig. 43. TLP with irregular waves (LC31): VRS predicted with 'w'.

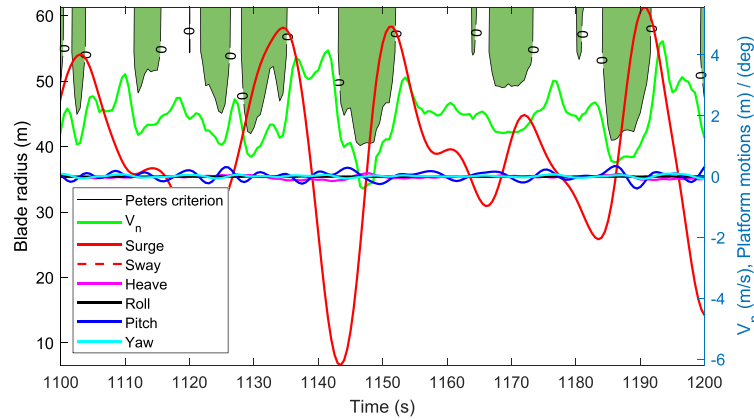


Fig. 44. TLP with irregular waves (LC31): VRS predicted with 'p'.

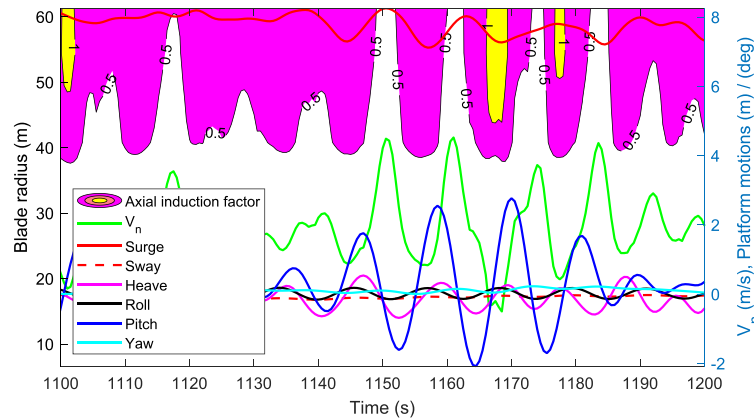


Fig. 45. Barge with irregular waves (LC1): VRS predicted with 'a'.

can either be dominated by surge or pitch motion. The VRS area predicted with 'p' totally cover that predicted with 'w' (see Fig. 28) (see Fig. 29) (see Fig. 30) (see Fig. 31) (see Fig. 32) (see Fig. 27).

4.1.4. Summary of regular wave load cases

The above analysis shows that the three different prediction

criteria agree in that the VRS area increase significantly with a decrease in wind speed and an increase in wave steepness. Fig. 34 and Fig. 35 further show the percentages of occurrence of VRS for the OC3 Hywind Spar wind turbine with a wave steepness of $\delta = 0.007$ and $\delta = 0.01$, respectively, over an operating time of 1200s. The different colors show different wind speeds, while the

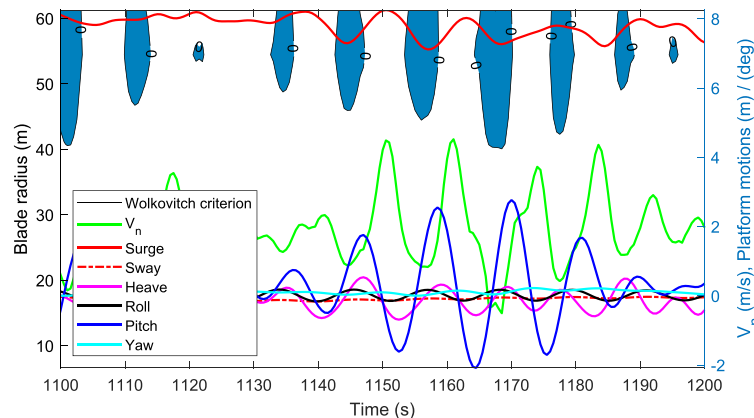


Fig. 46. Barge with irregular waves (LC1): VRS predicted with 'w'.

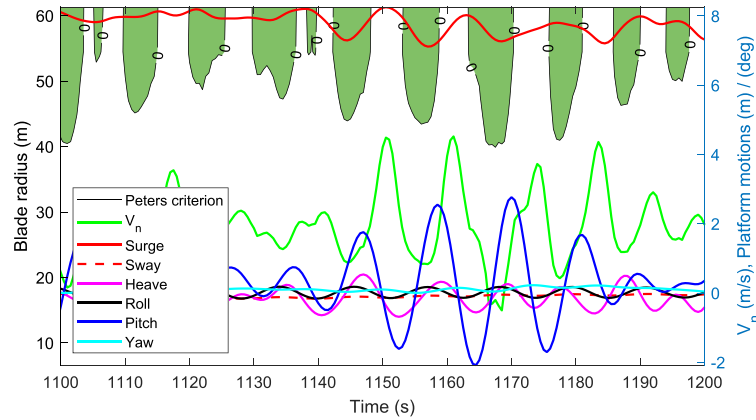


Fig. 47. Barge with irregular waves (LC1): VRS predicted with 'p'.

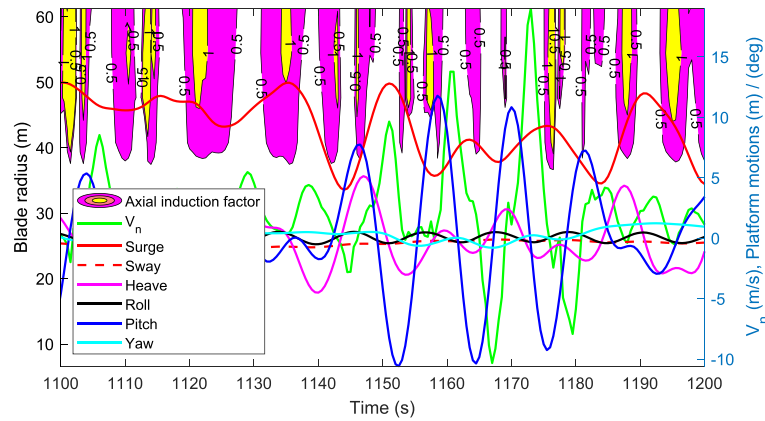


Fig. 48. Barge with irregular waves (LC16): VRS predicted with 'a'.

symbols relate to the different VRS criteria: axial induction factor a (\circ), Wolkovitch's criterion (\triangle) and Peters' criterion (\times). According to the criterion based on $a \geq 1$, the upper limits in terms of wind speeds for the VRS occurrence are $V_\infty = 8\text{m/s}$ for $\delta = 0.007$ and $V_\infty = 9\text{m/s}$ for $\delta = 0.01$. The maximum percentage of VRS occurrence is 29.48% for $\delta = 0.007$ and 30.14% for $\delta = 0.01$. Both

these values occur when $V_\infty = 4\text{m/s}$ and $H = 7\text{m}$. According to Wolkovitch's criterion, the upper limit in terms of wind speeds for the VRS occurrence is $V_\infty = 11\text{m/s}$ for both $\delta = 0.007$ and $\delta = 0.01$. The maximum percentage for $\delta = 0.007$ is 48.88% and for $\delta = 0.01$ is 49.04%, and they both occur when $V_\infty = 4\text{m/s}$ and $H = 7\text{m}$. According to Peters' criterion, the upper limit in terms of wind speeds

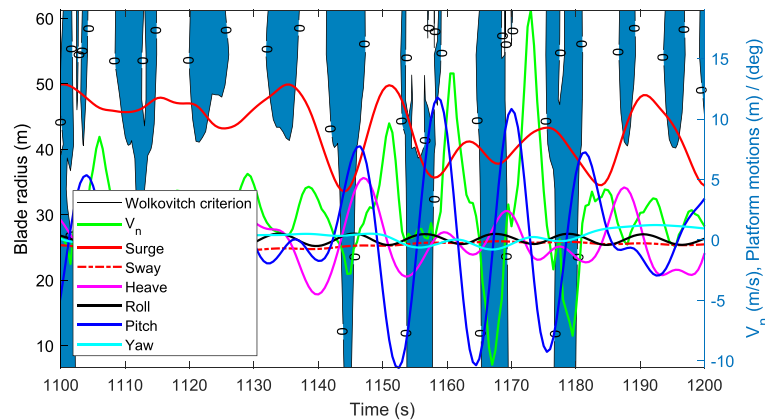


Fig. 49. Barge with irregular waves (LC16): VRS predicted with 'w'.

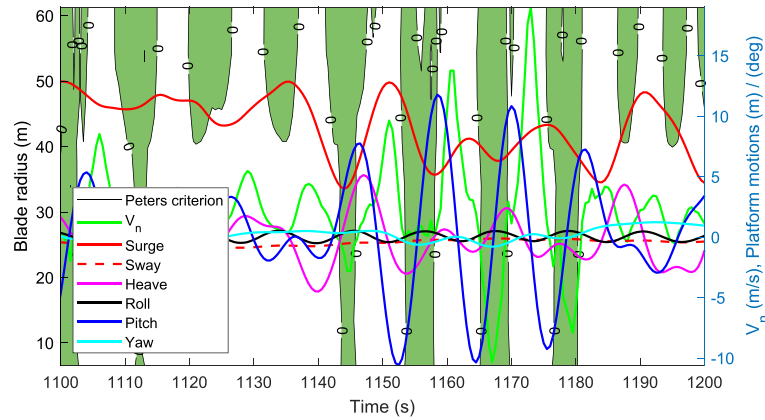


Fig. 50. Barge with irregular waves (LC16): VRS predicted with 'p'.

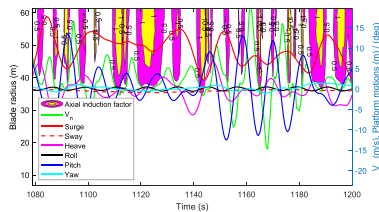


Fig. 51. Barge with irregular waves (LC31): VRS predicted with 'a'.

for the VRS occurrence is $V_\infty = 12\text{m/s}$ for both $\delta = 0.007$ and $\delta = 0.01$. The maximum percentage for $\delta = 0.007$ is 50.96% and for $\delta = 0.01$ is 50.79%, which both occur when $V_\infty = 4\text{m/s}$ and $H = 7\text{m}$. It can also be noted that the VRS area predicted by Peters' criterion is larger than that predicted by Wolkovitch's criterion, which is also larger than that predicted by the criterion based on the axial induction factor. This is because the axial induction factor predicts the very center of the VRS, which is between the turbulent wake state and the propeller state at $a = 0$. By contrast, Wolkovitch's criterion predicts the VRS when the rotor enters the core of the vortex ring. Therefore, it covers a larger area than only $a = 0$. Finally, Peters' criterion leads to a larger region than Wolkovitch's criterion as it predicts the boundaries of the VRS region and not only the center of the region.

4.2. Irregular wave load cases

4.2.1. NREL 5 MW turbine mounted on a TLP

The examples of the VRS prediction results for the NREL 5 MW turbine mounted on a TLP under irregular wave load cases are shown from Fig. 36 to Fig. 44 for the load cases LC1, LC16 and LC31. For the NSS load case (LC1), there is a large area of $a > 0.5$ but no VRS predicted with the axial induction factor. With 'w', there are small areas of VRS on the outboard of the blade, with a percentage of 11.74% in time series. Finally, Peters' criterion lead to larger area of VRS on the outboard of the blade, with a percentage in time series of 53.87%. In the ESS 1-Year load case (LC16), a small area of $a > 1$ is shown with a percentage of 4.66%, whilst 'w' gives a larger area with a percentage of 39.22% and 'p' leads to the largest area of VRS and a percentage of 51.87%. Similar trends can be found for the ESS 50-Year load case (LC31), with the percentages of occurrence of VRS of 10.16%, 41.3% and 51.37% according to the 'a', 'w' and 'p', respectively. According to Table 3, the natural period of the surge motion for the TLP is 60.6s, which is larger than the wave periods of the load cases considered here (see Table 5) and the natural period of the pitch motion is 4.5s, which is smaller than the wave periods. The results show that the low frequency surge motion of the TLP platform is more sensitive to the wave loads than the high frequency pitch motion. A further sensitivity analysis could help confirming this more broadly (see Fig. 38) (see Fig. 39) (see Fig. 40) (see Fig. 41) (see Fig. 42) (see Fig. 43) (see Fig. 37).

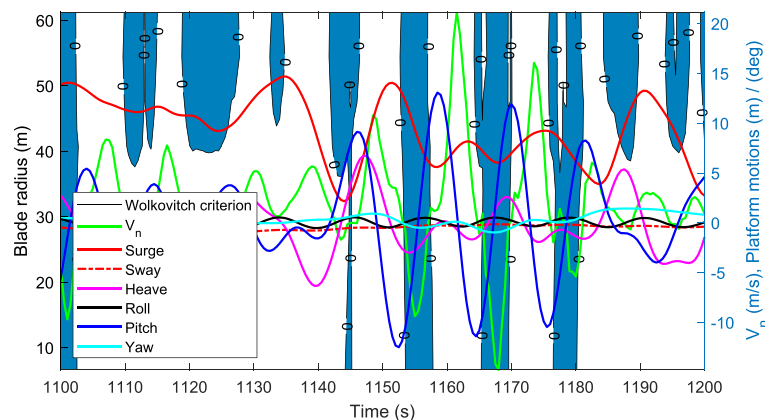


Fig. 52. Barge with irregular waves (LC31): VRS predicted with 'w'.

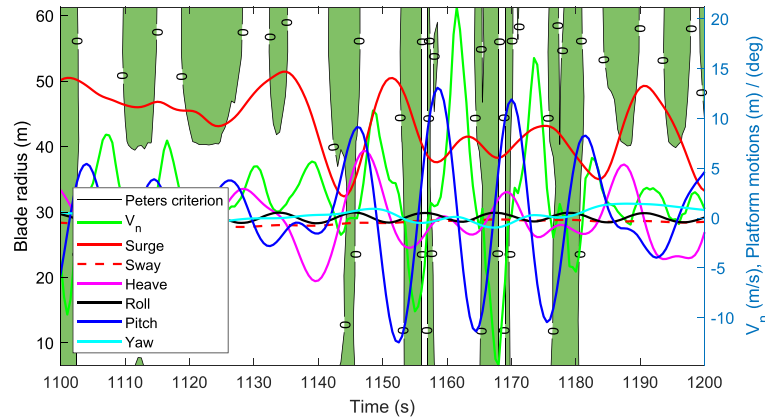


Fig. 53. Barge with irregular waves (LC31): VRS predicted with 'p'.

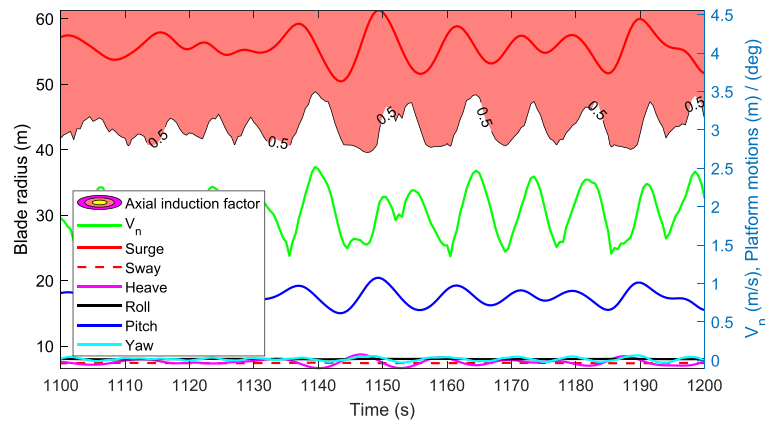


Fig. 54. Spar with irregular waves (LC1): VRS predicted with 'a'.

4.2.2. NREL 5 MW turbine mounted on the ITI Energy Barge

The examples of the VRS prediction results for the NREL 5 MW turbine mounted on the ITI Energy Barge under irregular wave load cases are shown from Fig. 45 to Fig. 53. For LC1, there is a large area of $a > 0.5$ and smaller areas of $a > 1$ with a percentage of 5.83%. The percentages become 40.38% and 56.62% based on 'w' and 'p',

respectively. These percentages increase for LC16 to 21.32%, 49.46% and 54.87% based on 'a', 'w' and 'p', respectively. A similar trend is found with LC31, with percentages of 19.48%, 47.38% and 51.54%, respectively. The ITI Energy Barge has a natural period in surge of 131.6s, which is larger than the wave periods, and a natural period in pitch of 11.8s. The results show that the surge and pitch motions

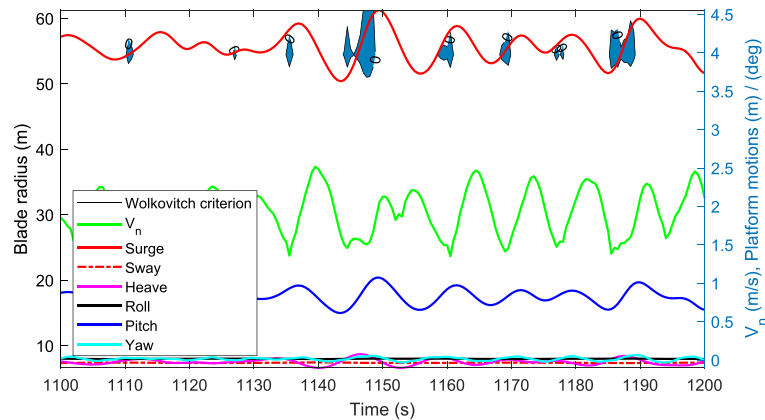


Fig. 55. Spar with irregular waves (LC1): VRS predicted with 'w'.

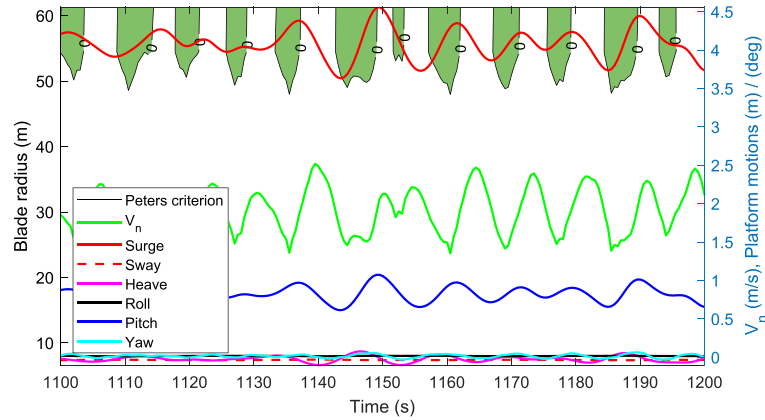


Fig. 56. Spar with irregular waves (LC1): VRS predicted with 'p'.

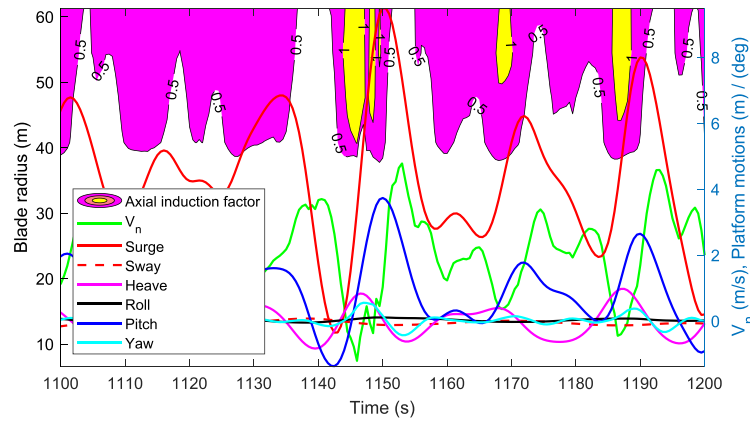


Fig. 57. Spar with irregular waves (LC16): VRS predicted with 'a'.

of the platform are both sensitive to the wave loads, while the pitch motion has a bigger impact on V_n . As opposed to the TLP results, the ITI Barge has lower percentages of occurrence of the VRS under the ESS 50-Year load case than under the ESS 1-Year load case. This is mainly because larger velocities of V_n fluctuation occur for the ESS 1-Year load case, despite the fact that the wave height of the ESS 50-

Year load case is bigger (see Fig. 47) (see Fig. 48) (see Fig. 49) (see Fig. 50) (see Fig. 51) (see Fig. 52) (see Fig. 46).

4.2.3. NREL 5 MW turbine mounted on the OC3-Hywind Spar

The examples of the VRS prediction results for the NREL 5 MW turbine mounted on the OC3-Hywind Spar under irregular wave

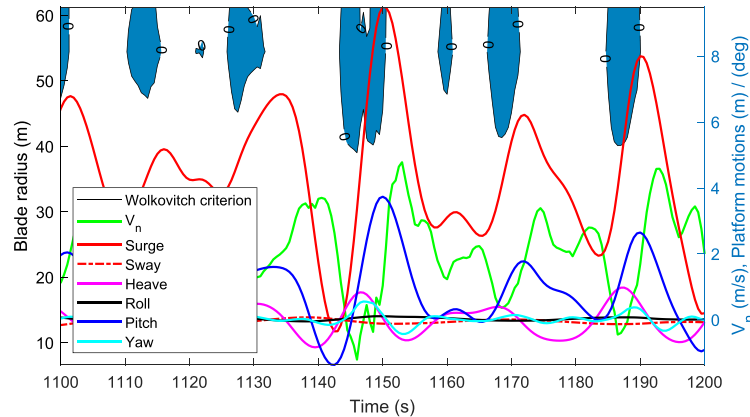


Fig. 58. Spar with irregular waves (LC16): VRS predicted with 'w'.

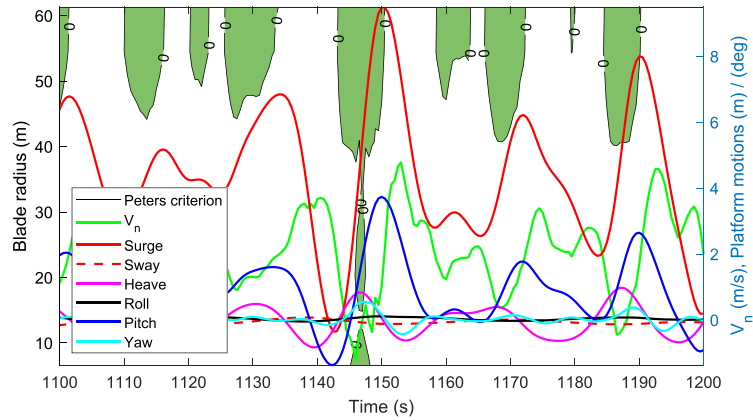


Fig. 59. Spar with irregular waves (LC16): VRS predicted with 'p'.

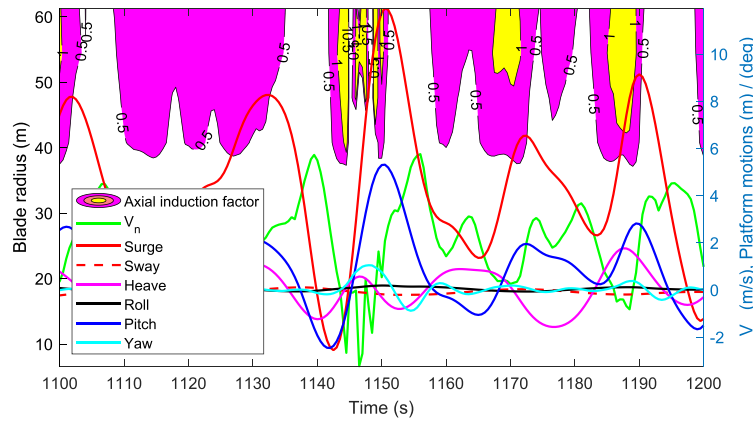


Fig. 60. Spar with irregular waves (LC31): VRS predicted with 'a'.

load cases are shown from Fig. 54 to Fig. 62. As for the TLP, the results based on the induction factor show no VRS for LC1. Based on 'w' and 'p', the percentages of occurrence of VRS are 18.07% and 53.96%, respectively. Again, the percentages increase with the load cases. Under LC16, these are 16.82%, 43.96% and 51.37% based on 'a', 'w' and 'p', respectively. For LC31, they are 21.23%, 45.05% and

52.21%, respectively. The natural period of the surge and pitch motions for the OC3 spar are 125.0s and 29.2s, respectively, which are both larger than the wave periods of these load cases. The results show that the surge and pitch motions of the OC3-Hywind Spar platform are both sensitive to the wave loads (see Fig. 56) (see Fig. 57) (see Fig. 58) (see Fig. 59) (see Fig. 60) (see Fig. 61) (see

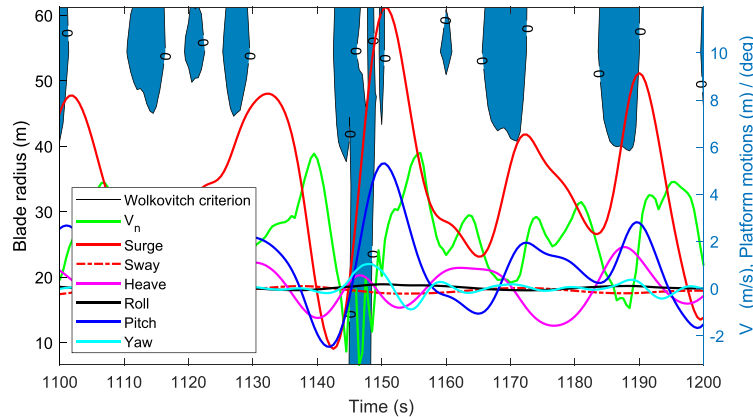


Fig. 61. Spar with irregular waves (LC31): VRS predicted with 'w'.

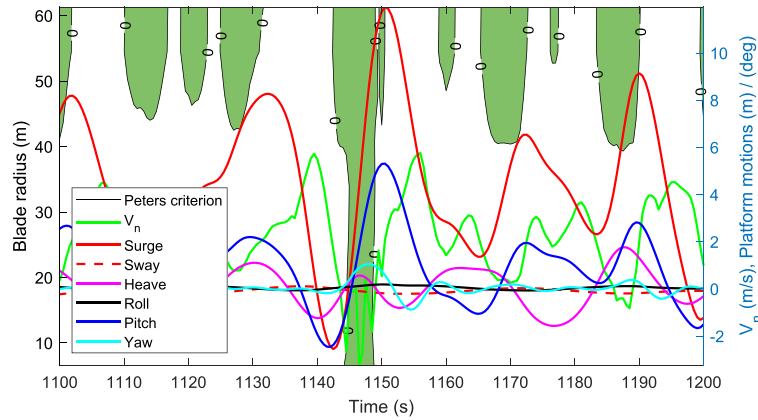


Fig. 62. Spar with irregular waves (LC31): VRS predicted with 'p'.

Fig. 55).

4.2.4. Summary of the results under irregular wave load cases

Fig. 63, Fig. 64 and Fig. 65 show the percentages of occurrence of the VRS for the different floaters under irregular wave state. The results show that the VRS mainly occurs for the design load cases in irregular wave states at low wind speeds. Generally speaking, for a given wind speed, the ESS 50-year load cases have a bigger risk of leading to the VRS than the ESS 1-year load cases. The NSS load cases exhibit the smaller risk of VRS occurrence. Exceptions are when large V_n fluctuations occur for small wave heights. Also, the different floating foundations respond differently to the same load case. For example, the ITI Energy Barge is the most sensitive one to waves, leading to a higher probability of occurrence of VRS. By contrast, the TLP exhibits the least motion and has thus the smallest percentage of occurrence of VRS in the three types of floating foundations. The VRS of floating offshore wind turbines is a periodic phenomenon, with an upper limit for the percentage of occurrence in the time series of around 50%.

4.3. Coefficient of variation analysis

The coefficient of variation, c_v , of the angle of attack (AoA) is

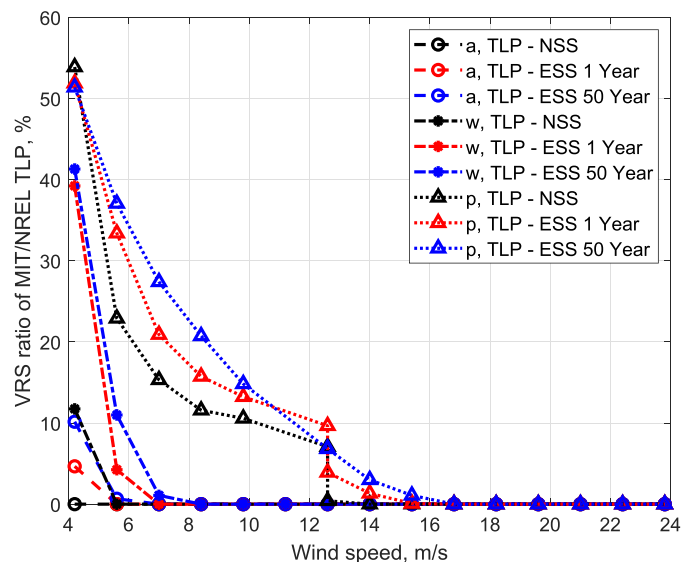


Fig. 63. Percentages of VRS for the MIT/NREL TLP in irregular wave state.

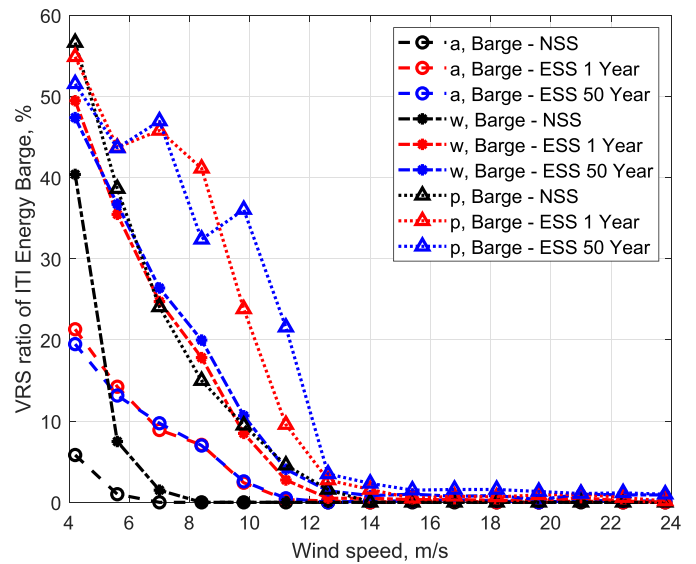


Fig. 64. Percentages of VRS for the ITI Energy Barge in irregular wave state.

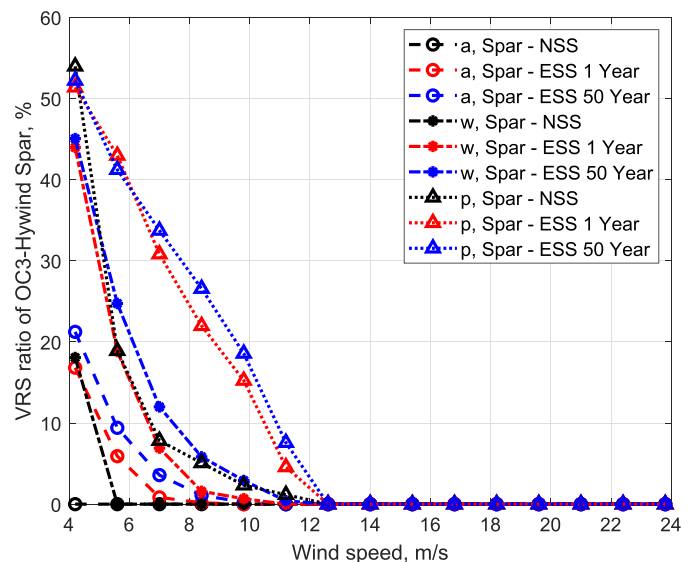


Fig. 65. Percentages of VRS for the OC3-Hywind Spar in irregular wave state.

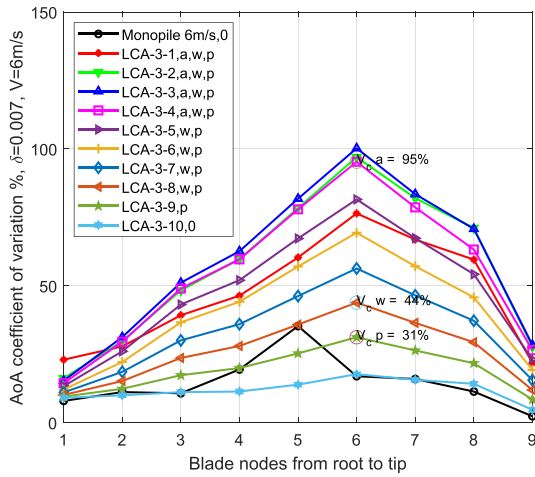


Fig. 66. AoA coefficient of variation %, $\delta = 0.007$, $V = 6\text{ m/s}$.

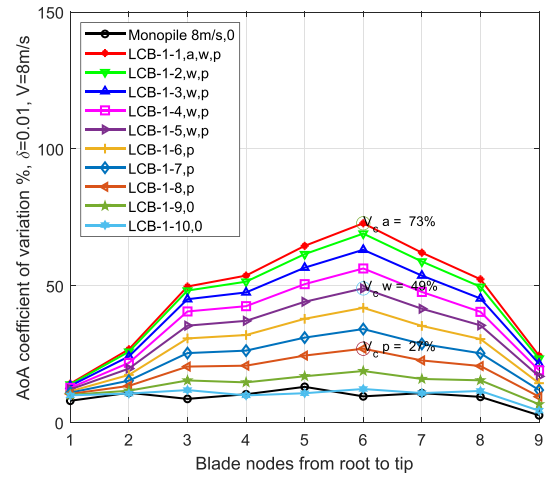


Fig. 68. AoA coefficient of variation %, $\delta = 0.01$, $V = 8\text{ m/s}$.

evaluated in this section. The coefficient of variation is a dimensionless measure of dispersion of a probability distribution defined as the ratio of the standard deviation σ and the mean μ , as

$$c_v = \frac{\sigma}{\mu} \tag{17}$$

As for the angle of attack, its coefficient of variation represents the level of its fluctuation frequency. Since the change of AoA will directly change the lift and drag force on the blade, the frequent change of AoA can be related to the fluctuation of aerodynamic loads on the blade. Here we discuss the load cases with wind speeds of 6 m/s and 8 m/s where stable positive angles of attack can be obtained along the whole blade of the bottom-mounted monopile wind turbine. The results are presented in Fig. 66 for design load cases of set A and Figs. 67 and 68 for design load cases of set B. In these figures, the prediction methods based on a , Wolkovitch and Peters criteria are denoted as 'a', 'w' and 'p', respectively. The load cases with no VRS predicted are marked with '0'. Interesting observations can be made. First, the c_v of the AoA increases with the decrease in wind speed. Also, for the same wind speed, the c_v of the AoA increases with the increase in wave steepness. Second, with the same wind speed and wave steepness, the c_v of the AoA increases with the increase in wave height. Third, the c_v of the bottom-mounted wind turbine always has a peak value in the

middle of the blade (node 5), while the peak values of the c_v for the FOWT shifts to the VRS region outboard of the blade (node 6). This agrees with Leishman's finding that, during VRS, the level of thrust fluctuations is high [10]. Fourth, the higher the c_v , the higher the chance of occurrence of VRS. We find that if the VRS occurs at a certain value of c_v , then the VRS also occurs when c_v is higher than the original one. In Figures 66–68, the peak c_v of load cases where the VRS occurs according to 'a', 'w' and 'p' for the first time are marked in the pictures.

Here we can see that 'a' leads to a c_v between 64% and 97%, 'w' gives c_v between 44% and 50%, and 'p' leads to a c_v between 22% and 31%. Thus it can be concluded that the induction factor 'a' is a very conservative method for the prediction of VRS, as the c_v for this prediction method is almost 3 to 4 times that of the bottom-mounted monopile wind turbine. However, it is a good quantity to assess when the BEM theory breaks down. By contrast, 'p' is the loosest of the three prediction methods, and can sometimes lead to a value of c_v that is lower than that of the bottom-mounted wind turbine. Finally, 'w' shows the strongest relationship with the value of c_v , where VRS is predicted with the peak c_v stably above approximately 40% and is clearly different than that of the monopile wind turbine. Accordingly, Wolkovitch criterion is the most suitable one for the VRS prediction, while Peters criterion indicates the initial aerodynamic change and is therefore more suitable for early warning of the occurrence of VRS during the operation of FOWTs.

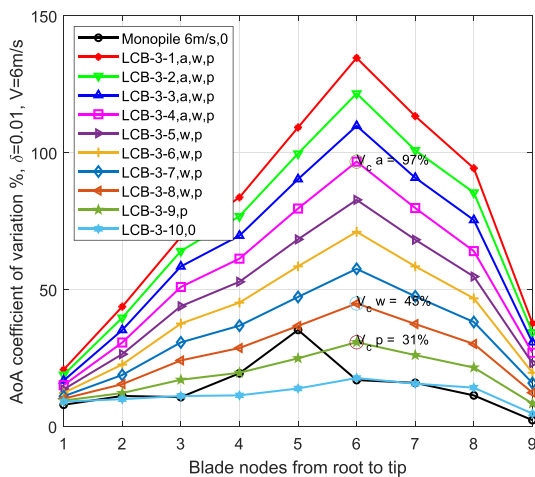


Fig. 67. AoA coefficient of variation %, $\delta = 0.01$, $V = 6\text{ m/s}$.

5. Conclusion and discussion

In this paper, the vortex ring state of floating offshore wind turbines is quantitatively predicted. Three criteria were used to predict the occurrence of VRS: the axial induction factor, Wolkovitch's criterion and Peters' criterion. The results show that the type of floating foundation has a significant influence on the aerodynamic performance of the rotor. As expected, the TLP exhibits the least motions, and therefore, also the least probability of occurrence of the VRS. Also, the probability of occurrence of VRS generally increases with the magnitude of the wave height, except in cases where the velocity normal to the rotor exhibits large fluctuations. However, importantly, for all the platform types, the turbine presents a risk of experiencing the vortex ring state even under normal sea states. This study can therefore be used as a basis to derive mitigation methods for the occurrence of VRS during operation. Finally, this study looks at the occurrence of VRS purely due to

platform motions, as the wind speed is assumed to be uniform. Additionally, both the blades and tower are assumed to be rigid. In future work, the effect of turbine aeroelasticity and changes in wind conditions could be taken into account. Also, the results are obtained for a specific site located on the North Atlantic Ocean, where the mean wind speed is relatively large throughout the year. The VRS phenomenon may be even more problematic at other locations, where the wind speeds are smaller.

6. Acknowledgements

Dong would like to acknowledge the support from China Scholarship Council (CSC). Many thanks to professor Carlos Simao Ferreira for his participation of the discussion about this research and sharing of his knowledge and experience with us. Special thanks are also given to Jason Jonkman of NREL for his valuable explanation of using FAST.

CRediT authorship contribution statement

Jing Dong: Conceptualization, Methodology, Software, Validation, Formal analysis, Investigation, Resources, Data curation, Writing - original draft, Writing - review & editing, Visualization, Project administration, Funding acquisition. **Axelle Viré:** Supervision, Project administration, Writing - review & editing, Resources, Investigation.

Declaration of competing interest

The authors declare the following financial interests/personal relationships which may be considered as potential competing interests: There is no such financial interests/personal relationships.

Jing Dong.

References

- [1] T. Sebastian, M. Lackner, Characterization of the unsteady aerodynamics of offshore floating wind turbines, *Wind Energy* 16 (3) (2013) 339–352, <https://doi.org/10.1002/we.545>.
- [2] J. Jonkman, Development of Fully Coupled Aeroelastic and Hydrodynamic Models for Offshore Wind Turbines, Tech. Rep. CP-500-39066, NREL, 2006.
- [3] J. Dong, A. Viré, C. Ferreira, Z. Li, G. van Bussel, A modified free wake vortex ring method for horizontal-axis wind turbines, *Energies* 12 (2019) 3900, <https://doi.org/10.3390/en12203900>.
- [4] M. Jeon, S. Lee, T. Kim, Wake influence on dynamic load characteristics of offshore floating wind turbines, *AIAA J.* 54 (11) (2016) 3535–3545, <https://doi.org/10.2514/1.J054584>.
- [5] B. Xu, Y. Yuan, T. Wang, J. Cao, Unsteady aerodynamic analysis for offshore floating wind turbines under different wind conditions, *Phil. Trans. Math. Phys. Eng. Sci.* 373 (2015), <https://doi.org/10.1098/rsta.2014.0080>.
- [6] K. Sivalingam, S. Narasimalu, Floating offshore wind turbine rotor operating state - modified tip loss factor in bem and comparison with cfd, *Int. J. Tech. Res. Appl.* 3 (5) (2015) 179–189.
- [7] C. Wu, V. Nguyen, Aerodynamic simulations of offshore floating wind turbine in platform-induced pitching motion, *Wind Energy* 20 (5) (2017) 835–858, <https://doi.org/10.1002/we.2066>.
- [8] T. Sant, Improving BEM-Based Aerodynamic Models in Wind Turbine Design Codes, Delft University of Technology, PhD thesis, 2007.
- [9] W. Durand, A. Betz, C. Wieselsberger, H. Glauert, C. Koning, A general review of Progress, under a Grant of the Guggenheim Fund for the Promotion of Aeronautics, Springer: Berlin.
- [10] J. Leishman, *Principles of Helicopter Aerodynamics*, Cambridge University Press, Cambridge, 2006.
- [11] T. Tran, D. Kim, The platform pitching motion of floating offshore wind turbine: a preliminary unsteady aerodynamic analysis, *J. Wind Eng. Ind. Aerod.* 142 (C9) (2015) 65–81, <https://doi.org/10.1016/j.jweia.2015.03.009>.
- [12] T. Tran, D. Kim, J. Song, Computational fluid dynamic analysis of a floating offshore wind turbine experiencing platform pitching motion, *Energies* 7 (8) (2014) 5011–5026, <https://doi.org/10.3390/en7085011>.
- [13] M. Jeon, S. Lee, S. Lee, Unsteady aerodynamics of offshore floating wind turbines in platform pitching motion using vortex lattice method, *Renew. Energy* 65 (2–3) (2014) 207–212, <https://doi.org/10.1016/j.renene.2013.09.009>.
- [14] R. Kyle, Alleviation of the vortex-ring state for floating offshore wind turbines using a modified blade-tip shape, ETP Conference, Wind session.
- [15] R. Kyle, Y.C. Lee, W.-G. Früh, Propeller and vortex ring state for floating offshore wind turbines during surge, *Renew. Energy* 155 (2020) 645–657, <https://doi.org/10.1016/j.renene.2020.03.105>.
- [16] P. Basset, C. Chen, J.R. Prasad, S. Kolb, Prediction of vortex ring state boundary of a helicopter in descending flight by simulation, *J. Am. Helicopter Soc.* 53 (2008) 139–151, <https://doi.org/10.4050/JAHS.53.139>.
- [17] J. Drees, W. Hendal, *Airflow through Helicopter Rotors in Vertical Flight*, Tech. Rep. NLL Report V. 1535, National Aeronautical Research Institute, 1949.
- [18] K. Washizu, A. Azuma, J. Koo, T. Oka, Experiments on a model helicopter rotor operating in the vortex ringstate, *J. Aircraft* 3 (3) (1966) 225–230, <https://doi.org/10.2514/3.43729>.
- [19] H. Xin, Z. Gao, A prediction of the vortex-ring state boundary based on model tests, *Trans. Nan Jing Univ. Aeronaut. Astronaut.* 11 (2) (1994) 159–194, <https://doi.org/10.4050/JAHS.53.139>.
- [20] M.D. Betzina, *Tiltrotor Descent Aerodynamics: A Small-Scale Experimental Investigation of Vortex Ring State*, American Helicopter Society 57th Annual Forum Proceedings, Washington, 2001.
- [21] J. Wolkovitch, Analytical prediction of vortex-ring boundaries for helicopter in steep descents, *J. Am. Helicopter Soc.* 17 (1972) 13–19, <https://doi.org/10.4050/JAHS.17.13>.
- [22] D. Peters, S. Chen, Momentum theory, dynamic inflow, and the vortex-ring state, *J. Am. Helicopter Soc.* 27 (3) (1982) 18–24, <https://doi.org/10.4050/JAHS.27.18>.
- [23] J.I.G. Leishman, M.J. Bhagwat, S. Ananthan, Free-vortex filament methods for the analysis of helicopter rotor wakes, *Journal of Aircraft - J AIRCRAFT* 39 (2002) 759–775, <https://doi.org/10.2514/2.3022>.
- [24] S. Newman, R. Brown, J. Perry, S. Lewis, M. Orchard, A. Modha, Predicting the onset of wake breakdown for rotors in descending flight, *J. Am. Helicopter Soc.* 48 (1) (2003) 28–38, <https://doi.org/10.4050/JAHS.48.28>.
- [25] A. Taghizad, L. Jimenez, Binet, D. Heuzé, Experimental and Theoretical Investigation to Develop a Model of Rotor Aerodynamics Adapted to Steep Descent, American Helicopter Society 58th Annual Forum Proceedings, Canada, 2002.
- [26] D. Eggleston, F. Stoddard, *Wind Turbine Engineering Design*, Van Nostrand Reinhold Company, New York, 1987.
- [27] B. Jonkman, J. Jonkman, *Fast v8.15.00a-Bjj*, Tech. rep, NREL, 2016.
- [28] P. Moriarty, A. Hansen, *Aerodyn Theory Manual*, Tech. rep, NREL, 2005.
- [29] J. Jonkman, S. Butterfield, W. Musial, G. Scott, Definition of a 5-mw Reference Wind Turbine for Offshore System Development, Tech. rep, NREL, 2009.
- [30] J. Jonkman, D. Matha, A quantitative comparison of the responses of three floating platforms, European Offshore Wind 2009 Conference and Exhibition NREL/CP-500-46726.
- [31] D. Matha, Model Development and Loads Analysis of an Offshore Wind Turbine on a Tension Leg Platform, with a Comparison to Other Floating Turbine Concepts, Tech. Rep. NREL/SR-500-45891, NREL, 2010.
- [32] J. Journée, W. Massie, *Offshore Hydromechanics*, first ed., Delft University of Technology, 2001.
- [33] G.L. Dnv, *Environmental Conditions and Environmental Loads*, Tech. Rep. Recommended practice, DNVGL-RP-C205, DNV GL, 2017.
- [34] I, 61400–3, *Wind Turbines – Part 3: Design Requirements for Offshore Wind Turbines*, International Electrotechnical Commission (IEC), Switzerland, 2009.
- [35] J. Jonkman, *Dynamics Modeling and Loads Analysis of an Offshore Floating Wind Turbine*, Tech. Rep. NREL/TP-500-41958, NREL, 2007.